Broadband visual stimuli improve neuronal representation and sensory perception

Elisabeta Balla[1,2,3], Gerion Nabbefeld[1,3], Christopher Wiesbrock[1,3], Jenice Linde[1,3], Severin Graff[1,3,4], Simon Musall*[1,3,4,5], Björn M. Kampa*[1,2,3]

[1] Systems Neurophysiology, Department of Neurobiology, RWTH Aachen University, Aachen, Germany
[2] JARA BRAIN Institute of Neuroscience and Medicine (INM-10), Forschungszentrum Jülich, Jülich, Germany
[3] Research Training Group 2416 MultiSenses – MultiScales, RWTH Aachen University, Aachen, Germany
[4] Institute of Biological Information Processing, Department for Bioelectronics, Forschungszentrum Jülich, Jülich, Germany
[5] Faculty of Medicine, Institute of Experimental Epileptology and Cognition Research, University of Bonn, Germany
These authors jointly supervised this work: Simon Musall, Björn M. Kampa

Correspondence should be directed to Björn Kampa, kampa@brain.rwth-aachen.de , and Simon Musall, musall@bio2.rwth-aachen.de.

Abstract

Natural scenes consist of complex feature distributions that shape neural responses and perception. However, in contrast to single features like stimulus orientations, the impact of broadband feature distributions remains unclear. We, therefore, presented visual stimuli with parametrically-controlled bandwidths of orientations and spatial frequencies to awake mice while recording neural activity in their primary visual cortex (V1). Increasing orientation but not spatial frequency bandwidth strongly increased the number and response amplitude of V1 neurons. This effect was not explained by single-cell orientation tuning but rather a broadband-specific relief from center-surround suppression. Moreover, neurons in deeper V1 and the superior colliculus responded much stronger to broadband stimuli, especially when mixing orientations and spatial frequencies. Lastly, broadband stimuli increased the separability of neural responses and improved the performance of mice in a visual discrimination task. Our results show that surround modulation increases neural responses to complex natural feature distributions to enhance sensory perception.

Introduction

Receptive fields of neurons in the primary visual cortex (V1) are sparse representations of the visual scenery and selectively respond to prominent features, such as the orientation of elongated edges. Yet, edge orientations in natural scenes are conditionally dependent on each other and appear as specific combinations of common orientations, especially horizontal and vertical edges[1,2]. The visual system has, therefore, likely evolved to be well-tuned to the statistics of these features in the natural environment and shows highly variable and non-linear responses to complex visual stimuli[2–4]. Natural scenes have been shown to improve stimulus-specific V1 population responses[5] and have also been used to improve models of visual motion detectors[6,7]. In fact, even individual V1 neurons respond with high specificity to different natural images and exhibit complex tuning properties that go far beyond what could be inferred by their responses to simple sine-wave gratings or Gabor patches[8,9]. The conventional approach of studying the neural encoding of visual information by using a limited set of simple visual stimuli is, therefore, inadequate to identify the key properties of neural responses in the visual system because it only covers a very small range of the possible visual feature distributions. An alternative approach is to use natural scenes or images to identify neural response features to complex stimuli that

match the statistics of the environment[10–12]. However, since natural images are not parametrically well-defined[13,14], very large sets of images and complex models are required to identify meaningful neural response features. Moreover, the presentation of large sets of images is often prohibited by the limited number of neural responses that can be obtained for each stimulus[8,9,15].

Different approaches have been employed to study the neuronal encoding of complex visual scenes. Quantification of natural images by using a bank of visual filters allows an analytical description based on different visual features, such as orientation, spatial frequencies, and their higher-order correlations[16]. These filters mimic the tuning properties and receptive fields of visual cortical neurons so that their outputs provide a simple model for cortical responses to natural images. The outputs from first and higher-order filters can then be used to synthesize new images with similar features to the original image and experimentally test neural responses and sensory perception. Experiments in humans[17], monkeys[18,19], and mice[20] have shown that these synthesized naturalistic textures can be perceived as similar to their natural counterpart, in particular when specific higher-order correlations of visual features are preserved. While this approach can break down natural images into a set of higher-order parameters, the entire parameter space is too large to be tested systematically and has mostly been linked to visual processing in higher visual areas (HVAs)[18–20]. How higher-order parameters affect neural responses to low-level features in V1, therefore, remains elusive[21]. In addition, the modulation of neural responses by stimuli extending to the area surrounding the receptive field of a visual neuron[22,23] is usually not considered in these algorithms.

An alternative approach focuses on identifying higher-order patterns in adjacent image pixels[24–26]. Studies in humans, monkeys, and rats have demonstrated perceptual sensitivity for different statistical orders of these pixel patterns with the psychophysics matching natural scene statistics[17,26,27]. Correspondingly, neurons in the primary and higher visual cortex are more sensitive to cardinal orientations, which are also overrepresented in natural scenes[2,28,29]. However, local pixel patterns only represent a limited aspect of natural scenes, and it remains unknown how responses to these patterns relate to more global distributions of orientations or spatial frequencies. This is particularly important in the context of surround modulation, where local stimuli within the receptive field of cortical neurons are strongly modulated by the surrounding context, both for simple grating stimuli but also for more complex natural scenes[30–37]. Correspondingly, spatial correlations have also been shown to play an important role in the perception of natural scenes[18–20].

Several studies also used visual noise stimuli to characterize neural responses to richer combinations of low-level stimulus features[38–40]. Interestingly, such broadband stimuli that contain a mixture of stimulus features increase neural responses, most likely due to the recruitment of additional neurons with diverse tuning preferences for stimulus orientations and spatial frequencies[29,38,39,41]. This suggests that broadening the bandwidth of any visual feature with specific tuning in cortical neurons, such as orientation or spatial frequency, might be beneficial to elicit stronger responses from a diverse population of visual neurons. Earlier modeling work also suggested that such a diverse population of responding neurons might provide a more accurate encoding of natural images and potentially improve

perceptual acuity[39]. However, it remains unclear which low-level features are most effective in increasing cortical network activity and if the tuning of individual neurons or other factors, such as surround modulation, are the most important contributors. Moreover, the extent to which heightened neural responses to broadband stimuli can truly enhance visual perception remains an open question.

To assess the impact of broadband stimuli on neural responses and sensory perception, we therefore performed neural recordings and psychophysical experiments in mice. We used random phase textures, so-called motion clouds[42], to create broadband visual stimuli of different orientation or spatial frequency bandwidths. Motion clouds allow the generation of parametrically well-defined stimulus sets with specific feature distributions that can approximate the distributions of natural images. We then used two-photon imaging in awake mice to measure the responses of V1 in layer 2/3, exhibiting diverse visual tuning properties to visual gratings[43–45]. Increasing the orientation bandwidth activated more V1 neurons and also increased their neural response amplitude. In contrast, increasing the spatial frequency bandwidth modulated the activity of individual neurons but did not increase the overall neural population response. A Gabor filter model showed that this was not simply explained by the orientation tuning of individual neurons but also by center-surround suppression. Follow-up experiments confirmed this prediction, showing a clear relation between lowered surround suppression and increased broadband responses across individual neurons. Using high-density electrophysiology, we also recorded from deeper cortical layers and the superior colliculus (SC) and found that neurons were strongly driven by mixed stimuli with large orientation and spatial frequency bandwidth. Lastly, we trained mice to discriminate either the orientation or spatial frequency of motion cloud stimuli and found that expanding the orientation, but not spatial frequency, bandwidth improved perceptual performance. Our results demonstrate that surround modulation is an important driver of increased neural responses to complex visual stimuli, suggesting that cortical processing and visual perception are optimized for visual stimuli that match the statistics of natural sensory inputs.

Results

Broad orientation bandwidth increases the recruitment and response amplitude of V1 neurons

Natural scenes contain edges with a broad range of orientations that can strongly vary in different spatial locations (Fig. 1a). To test how neurons in the visual cortex respond to different ranges of orientation distributions (orientation bandwidth), we designed different sets of motion cloud stimuli to approximate a sensible range of orientation bandwidths that are also found in natural images[2,46,47] (Fig. 1b). Broadband stimuli had a bandwidth of 45° to match the dominant orientation bandwidths of natural images (Fig. 1a)[2] while mid-range stimuli (25°) were chosen to be between broad- and narrow-range stimuli with a 5° bandwidth. All motion clouds had a central orientation of 0° and a central spatial frequency of 0.04 cpd to match the response tuning of neurons in mouse V1 and HVAs[29,48,49]. We then presented 5-s long, rightward drifting motion cloud stimuli (1Hz) in a pseudorandom order (with 5-s mean-gray inter-stimulus interval) to awake, head-fixed mice that were passively sitting in a tube.

Using 2-photon imaging, we then measured the neural responses of layer 2/3 neurons in V1, ubiquitously expressing the calcium indicator GCaMP6f (Fig. 1c, d). To evaluate the impact of different

orientation bandwidths on the number of responding neurons, we first used a one-sided Mann-Whitney U test ($p < 0.05$) to identify all neurons with a significant response for each stimulus condition against baseline. Where possible, we used a linear mixed effects (LME) model, which accounts for nested data from multiple animals, to test for significant differences across conditions. Then, we followed with a Bonferroni correction for the number of performed tests (see Methods).

Further, expanding the orientation bandwidth induced a more than two-fold increase in the number of visually-responsive neurons across all sessions (Fig. 1e), demonstrating that broader orientation bandwidth stimuli recruit a much larger population of neurons (normalized responding cell count, both tested against the narrow stimulus: mid range (25°) = 1.38 ± 0.09, LME model test against narrow, T = 4.64, $p = 4.9 \times 10^{-5}$; broad range (45°) = 2.2 ± 0.23, LME model test against narrow, T = 5.58, $p = 3.04 \times 10^{-6}$; mean ± s.e.m, n = 18 sessions from 9 mice. See also per mouse comparison in Fig. S1a. Percentage of visually responsive neurons over total neurons per session: narrow range = 11% ± 1%; mid range = 15% ± 2%; broad range = 21% ± 2%). In addition to increasing the total number of responding neurons, expanding the orientation bandwidth also strongly increased neural responses, which were largest for the broad orientation bandwidth (Fig. 1f, $\Delta F/F_{narrow}$ = 1.16% ± 0.04%; $\Delta F/F_{mid}$ = 1.44% ± 0.04%, Wilcoxon signed rank test against narrow, $p = 5.21 \times 10^{-12}$; $\Delta F/F_{broad}$ = 2.29% ± 0.06%, Wilcoxon signed rank test against narrow, $p = 5.25 \times 10^{-66}$, mean ± s.e.m., n = 1394 neurons from 18 sessions, 9 mice, see also per mouse comparison in Fig. S1b).

Expanding the orientation bandwidth, therefore, increased both the number and amplitude of stimulus-responsive V1 neurons. Interestingly, this increase in response amplitude was also seen in neurons that consistently responded to all orientation bandwidths (Fig. 1g). These common responders significantly responded to all bandwidths (one-sided Mann-Whitney U test, $p < 0.05$) but also strongly increased their response amplitude to broadband orientation stimuli (Fig. 1g, $\Delta F/F_{narrow}$ = 3.39% ± 0.14%; $\Delta F/F_{mid}$ = 3.67% ± 0.13%, Wilcoxon signed rank test against narrow, $p = 2.6 \times 10^{-3}$; $\Delta F/F_{broad}$ = 5.05% ± 0.22%, Wilcoxon signed rank test against narrow, $p = 2.1 \times 10^{-9}$, mean ± s.e.m., n = 252 neurons from 18 sessions, 9 mice). This indicates that the increase in neural response amplitude was not solely explained by the recruitment of additional neurons but rather by a general increase in neural responsiveness.

To further assess if increased neural responsiveness was due to the recruitment of broadband-selective neurons, we calculated a bandwidth selectivity index (calculated as the response difference between a preferred orientation bandwidth and the mean of the response to the other two bands, divided by their sum) and identified bandwidth-selective cells using a shuffle control (see Methods). Most bandwidth-selective neurons preferred broadband stimuli, while a smaller subpopulation preferred narrowband stimuli (Fig. S1d). This could indicate that additional neurons were recruited due to their orientation tuning being further away from the narrow 5° range while narrowband-selective neurons with close to 5° tuning would become unresponsive. However, surprisingly few neurons were significantly bandwidth-selective (n = 25, 7, 76 neurons for the narrow, mid, and broad range, respectively, versus 252 common responders), suggesting that increased responsiveness to broadband stimuli was not just driven by broadband-selective neurons.

156 Lastly, we compared the response amplitude of narrow- versus broadband-selective neurons to test if
157 higher broadband response magnitude was driven by stronger responses of broadband-selective
158 neurons or rather a general increase in responsiveness, as in the common responders (Fig. 1g). Here,
159 we used a less conservative approach to identify bandwidth-selective neurons by selecting all cells that
160 only significantly responded to either the narrow- or broadband condition (one-sided Mann-Whitney U
161 test, $p < 0.05$). As expected, each group had their strongest responses to either narrow- or broadband
162 stimuli but the response amplitudes in their respective preferred stimulus condition were almost similar
163 (Fig. 1h, maximum response mean ± s.e.m.: $\Delta F/F_{narrow}$ 3.36% ± 0.28%, n = 152 neurons, $\Delta F/F_{broad}$ =
164 3.60% ± 0.17%, n = 487 neurons; Wilcoxon ranked sum test for narrow versus broad, $p = 0.089$).

165 Together, these results show that broadband orientation stimuli strongly increase the number and
166 amplitude of neural responses. However, this effect appears to be due to a general increase in neural
167 responses instead of the recruitment of a broadband-selective subpopulation with a stronger visual
168 response magnitude.

169 **Expanding spatial frequency bandwidth does not increase V1 responses**

170 Similar to stimulus orientations, natural scenes also contain a large range of spatial frequencies. Spatial
171 frequency distributions in natural scenes follow a power law, with higher power in the low-frequency
172 bands for broad image features and lower power in the high-frequency bands for fine structural
173 details[28,46] (Fig. 2a). V1 neurons have also been characterized for their spatial frequency tuning[2,29,49],
174 so we tested if expanding the spatial frequency bandwidth of visual stimuli would affect neural
175 responses similarly to orientation bandwidths. We, therefore, created motion cloud stimuli with different
176 spatial frequency bandwidths (0.004 cpd, 0.04 cpd, and 0.4 cpd) with a vertical orientation, again
177 approximating the distributions in different natural scenes (Fig. 2a, b). Visual stimuli were presented
178 pseudo-randomly while measuring the activity of V1 neurons as described above (Fig. 2c, d).

179 In contrast to orientation bandwidth, expanding the spatial frequency bandwidth did not increase the
180 number of visually responsive neurons across sessions (Fig. 2d, e; normalized responding cell count
181 both tested against narrow condition: mid range (0.04 cpd) = 1.03 ± 0.1, LME model test against narrow:
182 T = 0.35, $p = 0.72$; broad range (0.4 cpd) = 1.3 ± 0.24, LME model test against narrow, T = 1.43, p =
183 0.16; n = 16 recordings from 9 mice. See also per mouse comparison in Fig. S1e. Percentage of
184 responsive neurons over total neurons per session: narrow range = 7% ±1%, mid range = 7% ± 2%;
185 broad range = 9% ±1%, mean ± s.e.m.). Correspondingly, we found no significant increase in the
186 response amplitude to the broad versus narrow spatial frequency bandwidth stimuli for all responsive
187 neurons (Fig. 2f; $\Delta F/F_{narrow}$ = 1.7% ± 0.1%; $\Delta F/F_{mid}$ = 1.9% ± 0.1%; Wilcoxon signed rank test against
188 narrow: $p = 0.09$; $\Delta F/F_{broad}$ = 1.9% ± 0.1%; Wilcoxon signed rank test against narrow: $p = 0.25$, mean ±
189 s.e.m, n = 888 neurons from 16 sessions, 9 mice, see also per mouse comparison in Fig. S1e). There
190 were also no differences in response amplitude across stimulus conditions for common responders
191 (Fig. 2g, $\Delta F/F_{narrow}$ = 4.9% ± 0.4%; $\Delta F/F_{mid}$ = 6% ± 0.5%, Wilcoxon signed rank test against narrow: p =
192 0.11; $\Delta F/F_{broad}$ = 4.6% ± 0.4%, Wilcoxon signed rank test against narrow: $p = 0.71$, mean ± s.e.m., n =
193 68 neurons).

194 A potential reason for the lack of increased responses to broadband spatial frequency stimuli could be
195 that V1 neurons already exhibit broad spatial frequency tuning, resulting in overlapping activation of
196 these neurons by different spatial frequency bandwidths[29]. This should result in a larger percentage of
197 neurons that consistently respond to all spatial frequency bandwidth conditions. However, a smaller
198 percentage of all stimulus responsive neurons were common responders for broadband spatial
199 frequency versus broadband orientation stimuli (11.2% versus 18.1%, respectively, Fig. 1g & 2g).
200 Moreover, neurons that were significantly bandwidth-selective against a shuffle control were more
201 common for broadband spatial frequency stimuli compared to broadband orientation stimuli (11.1%
202 versus 7.7%, respectively). Lastly, an equally large amount of these bandwidth-selective neurons
203 preferred either narrow- or broad-range stimuli, whereas mid-range selective neurons represented a
204 smaller subpopulation (Fig. S1h). Broadening spatial frequency bandwidth, therefore, induced an equal
205 amount of up and down-modulation of neural responses in differently tuned neurons, but the total
206 number and amplitude of responsive neurons remained unchanged. In line with this finding, we also
207 found a similar response amplitude when selecting only neurons that significantly responded to either
208 narrow- or broadband spatial frequency stimuli (Fig. 2h, maximum response mean ± s.e.m $\Delta F/F_{narrow}$ =
209 4.32% ± 0.33%, n = 133 neurons, $\Delta F/F_{broad}$ = 4.99% ± 0.45%, n = 132 neurons; Wilcoxon ranked sum
210 test for narrow versus broad: p = 0.52).

211 To further test if the tuning of individual neurons differed between orientation and spatial frequency
212 relative to the range that we used in the motion cloud stimuli, we performed additional recordings and
213 presented simple gratings with different combinations of orientation and spatial frequency (Fig. S2). We
214 tested the feature tuning to a range of orientations and spatial frequencies that were most prominent in
215 natural images and, therefore, used to create our visual stimuli (dashed lines in Fig. 1a, 2a). While we
216 observed diverse neural tuning to the presented gratings, the tuning width of responding neurons
217 covered a comparable range of orientations and spatial frequencies relative to the used orientation or
218 spatial frequency bandwidths. This further argues against the hypothesis that the lack of increased
219 neural responses to broadband spatial frequency stimuli was because of particularly broad spatial
220 frequency tuning that prevented further recruitment of specific subpopulations. Instead, stronger
221 responsiveness to broader orientation bandwidths appears to be a specific feature of V1 neurons that
222 does not generalize to spatial frequency.

223 **A Gabor filter model with surround suppression accurately predicts broadband responses**

224 A parsimonious explanation for the increased neural recruitment and responsiveness to broader
225 orientation bandwidth would be the additional recruitment of neurons with orientation tuning that is
226 outside of a narrow orientation bandwidth stimulus. However, our earlier findings, such as the increased
227 response amplitudes in common responders when expanding the orientation bandwidth (Fig. 1h) and
228 the lack of a corresponding effect for broadband spatial frequency stimuli, appeared to be at odds with
229 this hypothesis. To create a theoretical prediction on the relation between orientation tuning and the
230 corresponding responses to broadband orientation stimuli, we designed a rich Gabor-filter-based model
231 representing the receptive field properties of V1 neurons[38,50] (Fig. 3a, Fig. S3 and see Methods). The
232 Gabor filters covered the same range of orientations and spatial frequencies contained in our visual

stimuli (Fig. S3). In addition, we performed further recordings of responses to narrow and broad orientation bandwidth stimuli, for which we also measured the preferred orientation tuning. We then compared response amplitudes evoked by narrow and broad orientation stimuli, depending on the preferred orientation of V1 neurons (Fig. 3b, c).

As expected, responses to narrow bandwidth stimuli were related to orientation tuning, with neurons tuned to the 0° central orientation responding the strongest. In contrast, no clear tuning dependence was present for responses to the broadband orientation stimuli (Fig. 3b, c). The Gabor filter model also reproduced this general dependence of neural responses on orientation tuning (yellow lines show best-model fits). However, the simple "tuning only" model predicted a much stronger orientation dependence of response amplitudes than experimentally observed, especially for the narrow bandwidth responses of 0°-tuned neurons (Fig. 3b, c; $R^2_{\text{tuning only}} = -1.266$). Because narrow stimuli have a more regular spatial structure than broadband orientation stimuli, we hypothesized that this mismatch could be explained by the surround suppression of neural responses. We, therefore, added a modulation of the Gabor responses in the image center by responses of the spatially surrounding Gabors with the same orientation tuning (Fig. S4). This expanded "suppression" model accurately described the orientation dependence of neural responses to both narrow and broad orientation bandwidth stimuli and obtained a much better fit to the measured data (red lines show best-model fits; $R^2_{\text{suppresion}} = 0.584$).

Based on the response amplitudes towards narrow and broad orientation bandwidth stimuli, we also computed an "orientation response modulation index" (ORI RMI) as the difference between narrow and broad orientation bandwidth responses, divided by their sum. As hypothesized, the increase in ORI RMI was strongest for neurons with orientation tuning further away from the 0° central orientation (Fig. 3d, ORI $RMI_{-45°} = 0.12 \pm 0.04$, T = 2.79, $p = 0.01$; ORI $RMI_{-22.5°} = 0.08 \pm 0.04$, T = 2.11, $p = 0.04$; ORI $RMI_{0°} = -0.03 \pm 0.04$, T = -0.90, $p = 0.37$; ORI $RMI_{22.5°} = 0.10 \pm 0.04$, T = 2.4, $p = 0.02$; ORI $RMI_{45°} = 0.13 \pm 0.04$, T = 3.74, $p = 10^{-3}$; mean ± s.e.m., LME model test against zero, n = 11 recordings from 5 mice).

In agreement with the better fit to response amplitudes (Fig. 3b, c), only the surround model accurately predicted the broadband modulation of neural response amplitudes across all orientation tunings (Fig. 3d, red line, $R^2_{\text{suppresion}} = 0.395$). In contrast, the simple tuning-only model predicted a stronger decrease in neural response amplitude for neurons with 0° tuning that was not seen in the measured responses (Fig. 3d, yellow line $R^2_{\text{tuning only}} = -1.67$). Similar to neural response modulation, we also observed a clear increase in the recruitment of neurons with orientation tuning that was further away from the central 0° orientation (Fig. 3e). To account for this modulation of neural recruitment in the model, we linearly rescaled the model fit to response modulation, assuming that increased response amplitudes should translate into observing a larger fraction of responding neurons. Again, the model that included surround suppression obtained a more accurate fit of the experimental data as the tuning-only model ($R^2_{\text{tuning only}} = 0.563$, $R^2_{\text{suppresion}} = 0.889$).

As in our earlier recordings (Fig. 2), expanding the spatial frequency bandwidth did not have an impact on neuronal response amplitudes, irrespective of their orientation tuning (Fig. S5a, spatial frequency response modulation index (SF RMI): SF $RMI_{-45°} = -0.06 \pm 0.06$, T = -1.37, $p = 0.19$; SF $RMI_{-22.5°} = -0.06 \pm 0.05$, T = -1.38, $p = 0.18$; SF $RMI_{0°} = -0.12 \pm 0.07$, T = -1,37, $p = 0.08$; SF $RMI_{22.5°} = -0.03 \pm$

272 0.09, T = -0.41, p = 0.68; SF $RMI_{45°}$ = -0.01 ± -0.06, T = -0.17, p = 0.87, mean ± s.e.m., LME model
273 test against zero, n = 11 recordings from 5 mice). Correspondingly, we also found no changes in the
274 recruitment of visually-responsive neurons or a clear dependence on their orientation tuning (Fig. S5b).

275 Together, these results suggest that orientation tuning, as well as surround inhibition, are important
276 factors in understanding broadband response modulation in V1. Importantly, the model predicted that,
277 due to their more consistent spatial structure, surround suppression should be highest for narrow
278 bandwidth stimuli, which could explain the corresponding increase in neural responses to broadband
279 orientation stimuli as surround suppression is lifted.

280 **Surround modulation is crucial to predict broadband responses of individual neurons.**
281 To directly test the effect of orientation tuning and surround modulation on broadband responses of
282 individual neurons, we performed additional experiments where we presented a set of narrow and
283 broadband stimuli to awake 2NiellJ mice, expressing GCaMP6s in excitatory neurons (Fig. 4a). All
284 stimuli consisted of motion clouds with a central spatial frequency of 0.04 cpd and a 0° central
285 orientation (Supplementary Movies 1-4). The "narrow" condition consisted of motion clouds with narrow
286 spatial frequency and orientation bandwidth (0.004 cpd and 5°, respectively). The "SF" condition
287 consisted of broad spatial frequency and narrow orientation bandwidth stimuli (0.4 cpd and 5°), while
288 the "ORI" condition consisted of narrow spatial frequency and broad orientation bandwidth stimuli (0.04
289 cpd and 45°). Lastly, the "mixed" condition consisted of both broad spatial frequency and orientation
290 bandwidth (0.4 cpd and 45°) to assess their combined impact on neural responses (Fig. 4b). These
291 stimuli were presented either full-field, covering the entire screen, or restricted to the center of the
292 receptive field location for the majority of recorded neurons in each session. The size of the center
293 stimulus was 15° to match the maximally stimulating receptive field size of V1 neurons in layer 2/3[37]
294 (see also Fig. S6 and Methods). The average RF size of the population across all imaging sessions
295 was 30.45°±2.04°, ensuring that the center stimulus was placed within the receptive field of the center-
296 responding cells.

297 To also identify differences in the higher order features of these different stimulus conditions, we
298 quantified the salient orientations and stimulus regularity (linear predictability) in the center relative to
299 the surround by computing the raw coefficient correlation[16] (Fig. 4c). While expanding the spatial
300 frequency bandwidth still preserved the elongated structure of the underlying gratings, expanding
301 orientation bandwidth resulted in the emergence of irregular lattice-like structures, which were less
302 redundant than coherent elongated edges. Moreover, combining broad spatial frequency and
303 orientation bandwidth in the mixed condition abolished most regular structures, leading to a strong
304 decrease in stimulus predictability in the center from the surround. Furthermore, we found a clear
305 reduction in higher-order image structure, computed as coefficient magnitude statistics[16], in the mixed
306 condition (Fig. S7). Interestingly, higher-order structures were increased in the ORI condition, potentially
307 explaining its saliency to the V1 layer 2/3 population.

308 Similar to our earlier results, neural responses to broadband orientation, but not spatial frequency,
309 stimuli were larger compared to the narrow condition. The same effect was seen for the mixed condition,

which elicited similar responses to the ORI condition (Fig. S8, all full-field responding neurons). This effect was also largely independent of the animal's behavioral state: while running generally increased visual responses, responses to the ORI condition remained consistently larger than responses to the narrow condition during both running and resting trials (Fig. S9).

To isolate the impact of surround modulation on single-cell broadband responses, we selected neurons with a receptive field center that matched the location of the center stimulus and significantly responded to at least one of the center stimulus conditions (one-sided Mann-Whitney U test, $p < 0.05$, see Methods). In addition, we used pupil tracking to confirm that mice did not move their eyes, which could have changed the position of the neural receptive fields on the screen (Fig. S6). For full-field stimuli, these neurons showed increased response amplitudes for the ORI condition and a similar trend for the mixed condition (Fig. 4d, $\Delta F/F_{narrow}$ = 3.27% ± 0.5%; $\Delta F/F_{SF}$ = 2.56% ± 0.35%, Wilcoxon signed rank against narrow, $p = 0.11$; $\Delta F/F_{ORI}$ = 3. 76% ± 0.49, $p = 5.9 \times 10^{-5}$; mixed = 2.98% ± 0.32, $p = 0.08$; mean ± s.e.m., n = 378 neurons from 5 mice). Importantly, this effect was not seen when stimuli were presented only to the receptive field centers of the recorded neurons without visual stimulation of the surround. Here, neural responses were similar between the narrow and ORI conditions, while responses to the SF and mixed conditions were lower than narrow responses (Fig. 4e, $\Delta F/F_{narrow}$ = 4.42% ± 0.37%; $\Delta F/F_{SF}$ = 4.39% ± 0.52%, Wilcoxon signed rank against narrow, $p = 7.8 \times 10^{-3}$; $\Delta F/F_{ORI}$ = 4.56% ± 0.45%, $p = 0.66$; mixed = 4.47% ± 0.51%, $p = 0.013$; response amplitude mean ± s.e.m., n = 378 neurons from 5 mice). This suggests that broadband stimulation may not primarily increase neural responses by increasing the feed-forward inputs to diversely tuned neurons but rather through a reduction of surround inhibition. To estimate the impact of surround modulation, we computed a surround modulation index (SMI) for each condition, defined as the difference between the full-field and center response divided by their sum. The more negative the SMI index, the stronger the surround inhibition for a given neuron. We found clear surround inhibition for the narrow stimulus condition that was still present for broad spatial frequency bandwidth but significantly lower for the broadband orientation and mixed conditions (Fig. 4f, SMI_{narrow} = -0.04 ± 0.01; SMI_{SF} = -0.04 ± 0.01, Wilcoxon signed rank test against narrow, $p = 0.06$; SMI_{ORI} = -0.02 ± 0.01, $p = 2.28 \times 10^{-7}$; SMI_{mixed} = -0.02 ± 0.01, $p = 1.42 \times 10^{-5}$, surround modulation index mean ± s.e.m., n = 378 neurons from 5 mice). Expanding the orientation bandwidth, therefore, reduces center surround inhibition of cortical neurons, which could be due to the lower predictability of the receptive field center from the surround. The lower center responses for the SF condition also suggest that broadband spatial frequency stimuli provide weaker feedforward inputs to V1 neurons than narrow stimuli, which might also contribute to the lack of increased neural responsiveness to full-field SF stimuli.

To assess their respective importance, we then combined surround modulation, orientation tuning, and center responses to predict the broadband responses of individual neurons. We again used an LME model to account for mouse identity and included all three factors as regressors to predict broadband modulation for each stimulus condition (Fig. 4g; see Methods). Aside from orientation tuning, for each neuron, we also used SMI_{narrow} to indicate their surround modulation. To also include changes in feedforward input, we computed the center response difference between a given modality and the narrow condition. The model accurately predicted broadband modulation of individual neurons in all

three conditions (Fig. 4h). While all regressors made different contributions in each stimulus condition, surround modulation showed the strongest and most consistent impact for all broadband stimuli. Orientation tuning had a significant impact on the orientation bandwidth expansion, whereas the center enrichment had a smaller but more consistent impact for all conditions (Fig. 4h, i).

Together, these results show that surround modulation strongly contributes to neural responses to broadband stimuli. A potential mechanism for the increased responsiveness to broad orientation bandwidths could, therefore, not only be the recruitment of neurons with diverse orientation tuning but also a release from surround inhibition due to the reduced predictability of the receptive field center.

Broadband visual stimuli increase neural responses in cortical and subcortical areas.

Earlier work suggested that broadband stimuli have distinct effects on neural responses in different HVAs[40]. We, therefore, used widefield calcium imaging to measure the impact of narrow, SF, ORI, and mixed stimuli on different visual areas. We again recorded from awake mice, head-fixed on a wheel, and presented full-field stimuli while imaging cortical activity through the cleared intact skull. All data was aligned to the Allen Common Coordinate Framework[51,] and we additionally confirmed the location of V1 and HVAs using visual field sign mapping[49,52–54] (Fig. 5a). Presentation of the narrow stimulus resulted in strong activation of V1 and the surrounding HVAs (Fig.5b, top left). Visual responses were strongest in the left hemisphere, contralateral to the stimulus presentation, but we also observed some ipsilateral activity, especially in the binocular region of V1. Another cause for ipsilateral responses could also be reflections in the setup that reached the other eye. For our analysis, we focused on the visual areas in the contralateral hemisphere. Expanding either spatial frequency and/or orientation bandwidth resulted in increased cortical activity that was mainly restricted to V1 (Fig. 5b). To verify this, we also computed the difference between responses towards ORI and narrow stimuli for V1 and the secondary visual areas (Fig. 5c). Here, V1 displayed the strongest increase in responses for ORI versus narrow stimuli with 0.81% ± 0.08%, confirming that broadband modulation was more pronounced in V1 compared to the surrounding HVAs (mean ± s.e.m.; ORI versus narrow: p = 0.0048, T = 4.34, LME model, n=8 sessions from 4 mice). In particular, stimuli with broader orientation bandwidth evoked significantly higher activity in V1 compared to narrow or SF stimuli (Fig. 5d, mean V1 activity: $\Delta F/F_{narrow}$ = 1.90% ± 0.22%; $\Delta F/F_{SF}$ = 2.24% ± 0.14%, LME test against narrow: T = 1.73, p = 0.11; $\Delta F/F_{ORI}$ = 2.71% ± 0.25%, T = 4.34, $p = 7 \times 10^{-4}$; $\Delta F/F_{mixed}$ = 2.52% ± 0.17%, T = 2.82, p = 0.014, mean ± s.e.m., n = 8 recordings from 4 mice). However, responses to mixed stimuli were not stronger compared to broad orientation bandwidth alone (LME test for mixed versus ORI, T = -0.77, p = 0.45).

To further assess how expanding orientation and spatial frequency bandwidth modulates neuronal responses across all cortical layers, we then performed electrophysiological recordings in V1 using high-density Neuropixels probes[55] in awake mice (Fig. 5e, left). Mice were again moving on a wheel, and we presented the same stimuli as described above. All stimulus conditions induced a clear modulation of local field potentials (LFPs), with significantly increased response modulation during broadband stimulation compared to the narrow condition (Fig. 5e, right; mean LFP response difference to narrow across layers: ΔLFP_{SF} = 4.28μV ± 1.32μV, T = 3.71, p = 1.6×10^{-3}; ΔLFP_{ORI} = 6.44μV ± 2.82μV, T = 2.91, $p = 9.5 \times 10^{-3}$; ΔLFP_{mixed} = 9.72μV ± 2.6μV, T = 3.78, $p = 1.3 \times 10^{-3}$; mean ± s.e.m.,

389 LME model test against zero, n = 6 recordings from 3 mice). The earliest responses occurred in Layer
390 4 (300-500 µm), with the most pronounced subsequent activation in the deeper cortical layers. In
391 agreement with our two-photon imaging results in superficial layers, broadband orientation stimuli
392 induced stronger response modulation compared to broadband spatial frequency stimuli, which was
393 also consistent across all layers (Fig. 5f). However, surprisingly, expanding both orientation and spatial
394 frequency bandwidth resulted in much stronger responses in deeper cortical layers.

395 In agreement with our 2-photon results, we also observed a clear increase in neuronal responses to
396 broadband orientation stimuli in the spiking activity of superficial layer 2/3 neurons (Fig. S10a). To
397 compare the spiking response strength across the four stimulus conditions, we calculated the response
398 area under the receiver-operator characteristic curve. The AUC is a standardized measure for the
399 overall separability between the baseline and stimulus period and, therefore, equally sensitive to more
400 subtle sensory responses in sparsely active neurons. Unresponsive cells are represented by a value of
401 0.5, while values closer to 1 or 0 show reliable enhanced or suppressed responses, respectively. Neural
402 responses to the ORI condition were significantly stronger than the narrow condition (Fig. S10a,
403 AUC_{narrow} = 0.69 ± 0.01; AUC_{SF} = 0.68 ± 0.01, LME model test against narrow, T = -0.79, p = 0.43;
404 AUC_{ORI} = 0.73 ± 0.01, T = 2.72, p = 7 x 10^{-3}; AUC_{mixed} = 0.70 ± 0.01, T = 0.57, p = 0.57, mean ± s.e.m.,
405 n = 53 neurons from 3 mice). In agreement with our LFP results, the mixed stimulus condition evoked
406 larger spiking responses in deeper layers (500-1000 µm depth, Fig. 5f) with a corresponding shift in
407 AUC values (Fig. S10b, AUC_{narrow} = 0.70 ± 0.01; AUC_{SF} = 0.68 ± 0.01, LME model test against narrow,
408 T = -2.77, p = 5 x 10^{-3}; AUC_{ORI} = 0.71 ± 0.01, T = 0.94, p = 0.34; AUC_{mixed} = 0.73 ± 0.01, T = 2.96, p =
409 3 x 10^{-3}; mean ± s.e.m., n = 200 neurons from 3 mice).

410 To also capture visual responses beyond the cortex, we further extended our experiments and recorded
411 spiking activity in the SC, although we could not map the receptive fields of SC neurons (Fig. S11).
412 Interestingly, SC neurons responded much more strongly to the mixed stimulus condition and a smaller
413 extent to broadband orientation and spatial frequency stimuli compared to narrow stimuli (Fig. S11d,
414 AUC_{narrow} = 0.68 ± 0.02; AUC_{SF} = 0.68 ± 0.02, LME model test against narrow, T = 0.11, p = 0.91;
415 AUC_{ORI} = 0.70 ± 0.02, T = 1.10, p = 0.27; AUC_{mixed} = 0.82 ± 0.02, T = 5.44, p = 4.46 x 10^{-6}, mean ±
416 s.e.m., n = 46 neurons from 3 mice).

417 Together, these results show that increased cortical activation by broadband visual stimuli is mainly
418 restricted to V1. While superficial layers show a clear preference for broadband orientation, deeper
419 layers were also strongly activated by mixed stimuli with broadband orientation and spatial frequency.
420 Interestingly, this is also the case for the subcortical superior colliculus, which receives direct input from
421 the retina but also from deeper layers of V1.

422 **Neural discrimination capability is enhanced by broader orientation bandwidth.**

423 We next wondered if expanding orientation bandwidth also improves the neural representation of
424 sensory information, thus increasing the discriminability of different broadband stimuli from each other.
425 To test this hypothesis, we presented stimuli with a different central orientation (0° or 90°) or central
426 spatial frequency (0.04 cpd or 0.16 cpd) and measured the impact of expanding orientation or spatial
427 frequency bandwidth on the ability of neurons to discriminate between the central features, i.e., the

spatial frequencies will be discriminated while orientation bandwidth is expanded and vice-versa. (Fig. 6a, e). To avoid any ambiguity, we did not change the bandwidth of stimulus orientations or spatial frequency together but instead compared neural responses to the central feature while changing the bandwidth of the other. Similar to our previous results, expanding the orientation bandwidth with a central spatial frequency of 0.16 cpd also increased the number of visually responsive neurons with a 1.36 ± 0.14 fold increase compared to the narrow condition (Fig. 6b, T = 2.75, $p = 9 \times 10^{-3}$; LME test against 0; percentage responsive neurons over total neurons per session: narrow range (5°): 11% ± 1%, mid range (25°): 15% ± 2%, broad range (45°): 21% ± 2%, mean ± s.e.m, n = 18 sessions from 9 mice). The increase was lower with a central spatial frequency of 0.16 cpd compared to 0.04 cpd (LME test, T = 3.91, $p = 4.1 \times 10^{-5}$), potentially because higher spatial frequency stimuli were less efficient in driving neural responses which may have also reduced the impact of broadband response modulation (Fig. 4e). The amplitude of neural responses was also increased, demonstrating that expanding orientation bandwidth increases neural responsiveness, regardless of the central spatial frequency (Fig. 6c; orientation modulation index: ORI $RMI_{0.04cpd}$ = 0.17 ± 0.01, LME test against zero, T = 14.3, $p = 7.27 \times 10^{-45}$; ORI $RMI_{0.16cpd}$ = 0.06 ± 0.01, T = 4.3, $p = 1.53 \times 10^{-5'}$; mean ± s.e.m., n = 1345 neurons from 18 recordings from 9 mice). Such increased neural responsiveness to broadband stimuli might enhance the discriminability of different spatial frequencies by driving stronger responses in a larger population of V1 neurons. Conversely, broadband stimulation may also drive the same broadband-selective neurons irrespective of the central stimulus feature. However, neuronal responses to broadband stimuli with different central orientations or spatial frequencies were not strongly correlated, suggesting that most neurons respond differently to broadband stimuli when changing the central orientation or spatial frequency (Fig. S12).

To assess if expanding orientation bandwidth increases the neuronal discriminability between two central spatial frequencies, we computed a discrimination index (AUC_{abs}) as the absolute AUC between neural responses to stimuli with a central spatial frequency of either 0.04 cpd or 0.16 cpd (see also Fig. S13). AUC_{abs} was normalized between 0 and 1, with larger values indicating increased discriminability of the central spatial frequency and we computed the discriminability for either narrow or broad orientation bandwidth stimuli (Fig. 6d, $AUC_{abs,\ 5°}$ = 0.30 ± 0.01; $AUC_{abs,\ 45°}$ = 0.36 ± 0.01, LME model test against narrow condition, T = 8.13, $p = 5.44 \times 10^{-16}$; mean ± s.e.m., n = 2096 neurons from 18 sessions, 9 mice). The discriminability between central spatial frequencies was significantly increased with broader orientation bandwidth, demonstrating that broadband orientation stimuli increase cortical responses, which enhances the neural representation of other stimulus features.

In contrast, broadening the spatial frequency bandwidth did not increase the number or magnitude of neural responses to stimuli with a central orientation of either 0° or 90° (Fig. 6f, number of visually-responsive neurons compared to the narrow condition: broad SF bandwidth (90° central orientation) = 1.09 ± 0.21, T = 0.42, p = 0.67, LME model test against zero, mean ± s.e.m; Fig. 6g, spatial frequency modulation index: SF $RMI_{0°}$ = -0.004 ± 0.02, T = -0.17, p = 0.86; SF $RMI_{90°}$ = 0.014 ± 0.02, T = 0.6, p = 0.53, mean ± s.e.m., n = 16 recordings from 9 mice). Consequently, we found no significant change in the neural discriminability of stimuli with different central orientations when expanding spatial frequency bandwidth (Fig. 6h, orientation discrimination index: $AUC_{abs,\ 0.004cpd}$ = 0.30 ± 0.01; $AUC_{abs,\ 0.4cpd}$ = 0.32 ±

0.01, LME model test against narrow condition, T = 1.8, p = 0.06, mean ± s.e.m., n = 888 neurons from 9 mice).

Visual perception is improved by expanded orientation bandwidth.

Our results show that neural responses in V1 are enhanced when expanding orientation bandwidth, which also increases the neuronal discriminability of these broadband visual stimuli. To assess if increased neuronal discriminability also results in enhanced visual perception, we trained mice to perform a visual discrimination task while freely moving in a custom-built touchscreen chamber[28] (Fig. 7a). Here, mice had to discriminate between motion clouds by touching one of the two presented stimuli on a touch-sensitive screen and were rewarded when choosing the target stimulus. For two groups of mice (6 mice each), motion clouds either differed in their central spatial frequency (0.16 cpd target versus 0.04 cpd non-target; Fig. 7b, left, central orientation was 0° for both) or central orientation (0° target versus 90° non-target; Fig. 7b, right, central spatial frequency was 0.04cpd for both). In addition, we again varied the orientation or frequency bandwidth of the presented stimuli to test their impact on the animals' discrimination performance. As in our earlier experiments, the bandwidth was only altered for the stimulus parameter that was not tested in the discrimination task to avoid any ambiguity. In the orientation discrimination task, we thus varied spatial frequency bandwidth while varying orientation bandwidth during spatial frequency discrimination (Fig. 7b).

Animals were split into two groups and either trained on orientation or spatial frequency discrimination. Both groups reliably learned to perform their respective task and achieved comparable expert discrimination performance. Expanding the orientation bandwidth also improved the spatial frequency discrimination performance, demonstrating that broadband orientation stimuli not only improved neural response discriminability but also enhanced spatial frequency perception (Fig. 7c, percentage of correct trials: narrow (5°) = 77.0% ± 1.93%; mid range (25°) = 77.63% ± 1.62%, Wilcoxon signed rank against narrow condition: p = 0.92; broad (45°) = 82.77% ± 1.41%, $p = 4.9 \times 10^{-3}$, mean ± s.e.m., n = 46 sessions from 6 mice). Conversely, expanding spatial frequency bandwidth did not further improve orientation discrimination performance and even showed a trend towards reduced performance with higher spatial frequency bandwidth (Fig. 7d, percentage of correct trials: narrow (0.004 cpd) = 72.53% ± 2.85%; mid range (0.04 cpd) = 69.18% ± 2.12%, Wilcoxon signed rank test against narrow percentage of correct trials, p = 0.79; broad (0.4 cpd): 65.34% ± 3.60%, p = 0.29, mean ± s.e.m., n = 24, 16 and 18 sessions for each condition from 6 mice).

These findings strongly suggest that the enhanced neural discriminability of V1 responses translates into corresponding changes in visual perception, with the greatest discrimination performance observed for broad orientation bandwidths. However, a potential reason for the unchanged discrimination performance across spatial frequency bandwidths could be that perceptual changes are only visible near the frequency discrimination threshold, where even small perceptual variations can effectively impact behavior. We, therefore, further tested different spatial frequency bandwidths over a larger range of orientation differences (Fig. 7e). Using a staircase procedure, we dynamically changed the orientation difference between target and non-target stimuli to identify the orientation discrimination threshold for

each mouse within individual sessions. Consistent with our earlier results, the obtained discrimination thresholds and psychometric curves were similar across the tested spatial frequency bandwidths, again arguing against a notable impact of spatial frequency bandwidth on orientation discrimination (Fig. 7f, discrimination threshold at 72.7% orientation discrimination threshold from staircase procedure: narrow (0.004 cpd) = 46.54° ± 2.33°; mid range (0.04 cpd) = 49.93° ± 2.53°, Wilcoxon signed rank test against narrow, p = 0.61; broad range (0.4 cpd) = 49.34° ± 2.24°, p = 0.28, mean ± s.e.m, n = 18, 23 and 30 sessions respectively). Together, these findings show that broadband orientation, but not spatial frequency, stimuli can not only increase the responsiveness and discriminability of neural responses but also enhance visual perception.

Discussion

We used motion cloud stimuli with comparable bandwidths as in natural scenes to test the impact of broad orientation and spatial frequency bandwidth on neural responses and visual perception. Broadband stimuli elicited diverse V1 responses in awake mice, but only expanding orientation bandwidth increased V1 responses, reflected in more responsive neurons and larger response amplitudes (Fig. 1, 2). Aside from recruiting additional neurons with diverse orientation tuning, our modeling and experimental results showed that a key contributor to this effect is a broadband-specific reduction in surround inhibition (Fig. 3, 4). Moreover, our electrophysiological recordings show that mixed stimuli drive particularly strong responses in deeper cortical layers and the SC (Fig. 5), potentially due to their lower stimulus predictability. This prominent increase in response strength could be an adaptive mechanism of the visual system to enhance the perception of naturalistic broadband stimuli. Indeed, expanding the orientation bandwidth of visual stimuli also improved the discriminability of neural responses to visual stimuli with different spatial frequencies (Fig. 6). Lastly, we tested if such improved neural encoding is translated into enhanced visual perception and found that mice were more accurate in discriminating visual stimuli with broad compared to narrow orientation bandwidth (Fig. 7). Together, these results demonstrate that broadband stimuli engage V1 neurons by reducing surround inhibition, with orientation broadband stimuli increasing neural response strength, stimulus discriminability, and visual perception.

Our results of increased neural responsiveness to broadband orientation stimuli are in agreement with earlier work, showing that noise stimuli with broadband spatiotemporal frequencies and orientations can increase V1 responses[38,39]. An intuitive explanation for this effect is the additional recruitment of orientation-tuned neurons by stimuli that cover a broader range of orientations. To test this hypothesis, we used a computational model and found that orientation tuning is indeed a likely contributor to increased broadband responses. However, to accurately fit the measured response amplitude of orientation-tuned neurons, we also had to include response modulation by the stimulus surround. While the suppressive effect of narrow bandwidth grating stimuli that extend the receptive field size of cortical neurons has been well described[31,34,37,56], we found that broadband orientation stimuli release neurons from this surround suppression and thus enhance responses across a large fraction of the V1 population.

544 This difference in surround suppression could be due to a reduction in the predictability of the receptive
545 field center. When presenting natural images to awake monkeys, center-surround interactions in V1 are
546 sensitive to higher-order structures, such as image contours[57]. In contrast, randomizing the phases of
547 the Fourier spectrum of the image surround diminishes center-surround interaction, depending on the
548 inferred redundancies in the natural image[58]. Similarly, expanding the orientation bandwidth in random
549 phase motion clouds resulted in visual stimuli with a low raw coefficient correlation and, therefore, a low
550 predictability of the stimulus center by its surround[16]. In line with the predictive coding theory[59], stating
551 that responses in the receptive field center should be suppressed if they can be predicted by the
552 surround, we found that such reduced center predictability is indeed related to a reduction in surround
553 inhibition. Aside from feature tuning of individual neurons, center-surround modulation is, therefore, a
554 major driver of increased neural responses. Moreover, our results suggest that changes in surround
555 modulation are also likely to promote recently described response features of V1 neurons, such as
556 preferred responses to isotropic stimuli with shorter edges[40].

557 In contrast to orientation bandwidth, expanding the spatial frequency bandwidth had less impact on raw
558 coefficient correlation and surround suppression. Together with lower center responses, this difference
559 in stimulus predictability could also explain the selective increase in neural responses to broadband
560 orientation but not spatial frequency stimuli. Broader neural tuning to spatial frequencies compared to
561 orientations[29,48,49] might also result in an unselective activation of broadly responding neurons with
562 different spatial frequency bandwidths. If neurons were broadly tuned to spatial frequency, they would
563 be expected to respond to all spatial frequency bandwidth stimuli. However, our data show that they
564 are not tuned broadly relative to the tested spatial frequencies. When we directly compared the tuning
565 of V1 neurons to the same range of orientations and spatial frequencies that we used in our motion
566 cloud stimuli, the responses of individual neurons covered a largely similar range of stimulus bandwidths
567 for both features (Fig. S2). We also observed a larger proportion of cells responding to all orientation
568 bandwidth stimuli than to the full range of spatial frequency bandwidth motion clouds (Fig. 1g, 2g),
569 further suggesting that differences in neural tuning cannot explain the response preference to
570 broadband orientation stimuli.

571 Previous studies have shown that HVAs can be tuned to different spatial frequencies, to different
572 speeds, or show stronger orientation tuning[29,40]. Several areas are also more tuned to natural textures
573 than scrambled images or narrow bandwidth gratings[6,18]. We, therefore, used widefield imaging to
574 explore if areas outside of V1 show similar or stronger tuning to broadband visual stimuli. However,
575 broadband response modulation was strongest in V1, demonstrating its importance for processing
576 broadband stimuli. Our electrophysiological measures from deeper cortical layers and the SC also
577 showed that expanding orientation and spatial frequency bandwidths together can further increase
578 neural responses. The lower impact of spatial frequency bandwidth might, therefore, be specific to the
579 supragranular V1 layers. The stronger response modulation to the mixed stimulus condition in the
580 deeper LFP but also the widefield recordings could be explained by dendritic signals of layer 5 neurons,
581 which also contribute to widefield signals[60]. We also found stronger responses to broadband spatial
582 frequency compared to narrow stimuli in the LFP and widefield which were not seen in the 2-photon
583 and spiking recordings. A potential reason for this difference could be that LFP and widefield are

population measures that also represent dendritic and axonal signals that may not be reflected in somatic spiking. It is therefore possible that broadband spatial frequency stimuli have a more subtle impact on V1 inputs that was not detected in our single-cell measures of V1 neural activity.

Superficial V1 layers have also been implicated with processing prediction errors during motor-visual mismatch[61–64], stimulus sequences[65], and between center and surround[30,36,37]. In contrast to the preponderance of prediction-error neurons in layer 2/3, the deeper layer 5 has been implicated with the representation of the internal predictions[64,66]. Furthermore, V1 neurons have an additional receptive field in the surround with different visual tuning properties compared to the center receptive field[37]. The interaction of center and surround is thought to be tuned to the characteristics of natural scenes and might enhance natural pattern completion[67] which could explain the observed layer-dependence in responses to broadband visual stimuli. Co-stimulation of the center and the surrounding receptive field also lead to sparser neuronal responses and increased information coding[32–34,68] due to local network interactions that sharpen recurrent excitation to produce specific and reliable visual responses[33]. Together, increased neural responses to broadband orientations appear to be a specific feature of the visual cortex and could be an adaptation to the orientation distributions in natural scenes.

Superposition of differently oriented gratings can suppress cortical responses in anesthetized cats[69–73] and monkeys[39], while facilitated responses have been reported in awake monkeys and mice[40,74–79]. Surround suppression has been shown to be strongly reduced under anesthesia[31,37]; therefore, a release from surround suppression by broadband visual stimuli might be less effective. The large variety in cortical responses to multiple superimposed gratings could also be explained by orientation-specific horizontal interactions within V1[74,75,80] or a thalamocortical feedforward mechanism[77]. Furthermore, motion cloud stimuli have been used in human studies to test how visual speed processing depends on spatial frequency bandwidth[81]. While visuomotor reflexes were enhanced, perceptual speed discrimination was impaired for stimuli with large bandwidths. Since mice also possess speed-tuned neurons in the visual cortex[29,82], it would therefore be interesting to also test speed perception in mice using different bandwidth-enriched stimuli. Moreover, visual flow patterns of small moving bars evoke strong cortical responses that are different from those evoked by gratings and are also evoked at much higher spatial frequencies[83]. This suggests an additional mode of perception for global motion patterns, which might be related to our observation of increased responses to broad bandwidth motion clouds[80,83].

Theoretical studies using convolutional neural networks (CNNs) also showed that including surround suppression can considerably improve both the performance and training speed of traditional CNNs in visual tasks, showing a superior generalization capability in different lighting conditions[84]. Interestingly, we found that broadband orientation stimuli also improved spatial frequency discrimination, arguing that lower stimulus predictability can improve the sensory perception of specific visual features. Heightened sensory perception also depends on the saliency of a visual stimulus, which can be influenced by its surround, allowing it to merge or pop out from the rest of the visual scene[30,36,85–87]. This pop-out effect is even stronger in the SC[88] which is known to encode a saliency map of visual scenes primates[89]. Our finding that SC neurons strongly respond to heterogeneous broadband visual stimuli with low spatial correlations could suggest that less-predictable stimuli are also of higher saliency and, therefore, recruit

SC circuits more strongly than the visual cortex. An interesting topic for future studies would, therefore, be a more detailed comparison of cortical and subcortical processing of broadband stimuli.

Natural vision is broadband vision, and gratings of a single orientation and spatial frequency are rarely present in a natural environment. The visual system is tuned to the statistics of natural inputs[2,3], which is represented in the ability of mice and humans to discriminate fine differences in visual features that are most common in the environment[2,29,90]. Natural scenes also consist of distributions of largely overlapping orientations around areas of interest[1] (Fig. 1a), leading to complex receptive fields of cortical neurons that respond more strongly to visual features when they are embedded in natural scenes instead of random or artificial backgrounds[91]. Revealing the computational principles of natural scene processing is therefore crucial in order to understand visual processing at large. Our results with broadband orientation motion clouds demonstrate that rich but parametrically controlled visual stimuli are a promising tool to achieve this goal and reveal how the visual cortex has evolved to perceive our natural environment.

Methods

Animals. All experiments were carried out in accordance with the German animal protection law and local ethics committee (LANUV, NRW) under the study protocols 84-08.04.2016.A357 and 81-02.04.2021.A021. All mice (*Mus Musculus*) were between 14-30 weeks old. For the two-photon imaging experiments, six male and three female C57BL/6J (Charles River, Germany) mice (Fig. 1 and 2 show data from the same 9 mice, but each protocol was run separately on different days in randomized order) and five 2Niell/J (B6; DBA-Tg(tetO-GCaMP6s)2Niell/J, Charles River, Germany) females (Fig. 3 and 4) were used. For the widefield imaging experiments, two male and two female 2Niell/J mice were used. For the electrophysiological recordings, three 2NiellJ males were used. For the behavioral discrimination tasks, three female and three male C57BL/6J mice were used for the spatial frequency discrimination task; for the orientation discrimination task, six male C57BL/6J mice were used. All mice were kept on a reverse light cycle (light/dark cycle: 12/12 hours) with regulated temperature and humidity conditions (23 ± 2°C, 55 ± 5 % air humidity). Mice in the behavioral task were water-restricted throughout the experiments. They received water ad libitum on the weekend when no experiments were performed and received at least 1.5 ml of water on experimental days. Mice had access to food ad libitum and were weighed and checked for their health status before the start of each behavioral session.

Surgical procedures. For the cranial window implantation and viral injection, the mice were weighed and given a subcutaneous injection of Carprofen (4 mg/kg, Rimadyl, Zoetis GmbH) and Buprenorphine (0.1mg/kg, Buprenovet sine, Bayer Vital GMBH) for analgesia, 20 minutes before the surgical procedure. They were then anesthetized using (1%-2.5%) isoflurane in oxygen and placed in a stereotaxic frame with stabilized and monitored body temperature (37°C). Eye ointment (Bepanthen, Bayer Vital GmbH) was placed on the ipsilateral eye and ophthalmic gel in the contralateral to keep them moisturized but also allow intrinsic imaging to identify the location of V1[29,48,52,54]. Following a local injection of Bupivacaine (0.08ml of 0.25% Bucain 7.5mg/ml, Puren Pharma GmbH), the skin was incised and pushed aside to reach the skull around the position of V1, based on anatomical coordinates (3.5 mm posterior and 2.5 mm lateral from bregma). The skull was then carefully thinned with a dental drill to gain optical access to the cortex for intrinsic imaging (see section 'Intra-surgical intrinsic imaging'). A 4-mm-wide circular craniotomy was then performed over the center of V1. In the C57BL/6J mice for two-photon imaging, a viral vector (AAV9.Syn.GCaMP6f.WPRE.SV40; Addgene, viral titer ~10^{13} vg/ml, diluted 1:10 in phosphate-buffered saline (PBS)) was then injected through a thin glass pipette with a micropump (UMP-3, World Precision Instruments). In each mouse, we injected 250 µl at 100 nl/s in two separate V1 locations (~500µm apart from each other) to obtain an even expression GCaMP6f throughout the area (We waited around three weeks for stable expression before imaging). The dura was kept moist with PBS solution throughout the injection. After viral injections, a 4-mm-wide round coverslip was placed inside the craniotomy and fixed with light-curable dental cement (DE Flowable composite, Nordenta). For electrophysiology experiments, we used coverslips with a small opening (~0.2 mm) that was covered with silicon to allow access of the Neuropixels probes to the cortex. A metal head holder was then positioned and attached with dental cement to allow subsequent head fixation

675 and imaging in the two-photon microscope setup. In the 2Niell/J mice for the two-photon experiments,
676 the head-bar placement followed immediately after the window placement, and the location of V1 was
677 identified later with widefield field sign mapping (see section 'Widefield imaging'). The custom stainless
678 steel headbar piece was held in place with quick adhesive cement (Superbond C&B, Sun Medical CO.,
679 LTD) and fast-curing acrylic resin (Jet Denture repair, Lang Dental INC). For widefield imaging, 2Niell/J
680 mice were similarly prepared, but a skull clearing procedure was performed instead of the cranial
681 window[92]: the skull was thoroughly cleaned and covered with a thin, transparent layer of cyanoacrylate
682 (Zap-A-Gap CA+, Pacer technology) to obtain optical access to the cortical surface[93].

683 After the surgery, all animals received the same injections of Carpofen and Buprenorphine as in the
684 beginning and were kept over a heating blanket during their immediate recovery. They also received
685 Buprenorphine (0.009 mg/ml, Buprenovet sine, Bayer Vital GmbH) and Enrofloxacin (0.0227 mg/ml,
686 Baytril 5%, Bayer Vital GMBH) in their drinking water for three days. The recovery time was at least one
687 week before starting animal handling.

688 **Intra-surgical intrinsic imaging.** During cranial window surgeries, retinotopic mapping was performed
689 using intrinsic signal optical imaging to functionally confirm the location of V1. Here, we presented
690 continuous periodically drifting bars with a high contrast flickering checker pattern[49,52]. Stimuli were
691 created using Psychtoolbox[94,95] in MATLAB (MATLAB R2019b, MathWorks) and composed of a static
692 checker pattern with a patch size of 20° and contrast reversal at 3Hz. This pattern was masked and
693 only visible through a 15°-wide bar aperture, moving over the screen with a temporal period of 18
694 seconds in all four cardinal directions in randomized order. Stimuli covered roughly 120° horizontally
695 and 80° vertically and were pre-rendered in advance. A spherical correction was applied to compensate
696 for distortions due to the presentation on a flat monitor[49]. The monitor (BenQ XL2420T) was positioned
697 at an angle of 20° to the midline and tilted 10° above the animal. The eye was positioned at the
698 horizontal center of the monitor, 30 mm above the lower edge of the monitor, and the stimulus
699 presentation was adjusted accordingly. A vessel image for alignment was captured under green-light
700 illumination (peak ~525nm, green power LED, 15506, LUMITRONIX). Hemodynamic signals were
701 acquired under red-light illumination (peak ~630nm, red power LED, 15607, LUMITRONIX). Images
702 were captured using a tandem-lens macroscope composed of a 25 mm objective (DO-2595, Navitar)
703 above the subject and a 50 mm objective in front of a CMOS camera (acA1920-155um, Basler). In
704 between, a removable bandpass filter was used to isolate reflected red light (630 nm – 760 nm,
705 G384082035, Qioptiq). Phase maps of horizontal and vertical retinotopy were generated online using
706 custom software based on previously published analysis[54]. Visual field sign maps, delineating the
707 precise borders of V1 to higher visual areas, were then computed after imaging was completed[52]. During
708 intrinsic imaging, anesthesia was kept light, just above 1% isoflurane in oxygen. Throughout retinotopic
709 mapping, the state of anesthesia was closely monitored using an additional camera viewing the animal,
710 as well as screening for global drifts in the hemodynamic signal.

711 **Two-photon imaging.** Two-photon imaging was done in a custom-built setup with a resonant-scanning
712 two-photon microscope (CRS 8KHz, Cambridge Technology) and a femtosecond-pulsed TI: Sapphire
713 laser (Mai Tai DeepSee, Spectra-Physics) tuned to 920 nm. Data acquisition and controls were

714 performed with the MATLAB-based Scanimage package (Scanimage 2015)[96]. Settings and laser power
715 were kept constant across all mice and experiments. References from the vessel image, visual field
716 sign maps, and/or injection site referencing were used to define the center of the primary visual cortex.
717 Recordings were made from a single plane in layer 2/3 of V1 at a depth of 250-300 µm below the pial
718 surface with a frame rate of 30 Hz. We used a 16x, 0.8 NA Nikon objective lens (CFI75 LWD 16X W)
719 at a pixel resolution of 512 x 512 pixels (575 µm × 575 µm). Motion Cloud stimuli from the orientation
720 bandwidth expanding and the spatial frequency bandwidth expanding protocol (Fig. 1, 2, and 6, see
721 'Visual stimulation' section below) were presented at 17 cm distance from the right eye on a gamma-
722 corrected LED-backlit LCD monitor (BenQ XL2420T, 24", 60Hz refresh rate, or Viewsonic VX3276-2K-
723 MHD-2, 32", 60Hz refresh rate). The larger screen was used to increase the visual field coverage for
724 center-surround stimuli, where we also used a sparse noise stimulus[97] to map the preferred RF
725 locations of the individual neurons in the field of view of each recording. Two behavior cameras (Firefly
726 DL Teledyne FLIR) recorded the animal from different angles throughout the sessions for movement
727 and eye tracking.

728 **Widefield imaging.** Widefield Ca^{2+}-imaging was performed using a custom tandem-lens macroscope[98],
729 consisting of two 85 mm objectives (Walimex Pro 85mm f/1.4 IF; Walimex) using a sCMOS camera
730 (Edge 4.2, PCO) through the cleared intact skull. Frames were acquired using the Python-based
731 software package Labcams (Version 0.2 https://github.com/jcouto/labcams, by Joao Couto) at a
732 framerate of 30 Hz with an effective resolution of 512 x 512 pixels with 4 x 4 spatial binning. Frames
733 were acquired under alternating illumination using a blue LED (470 nm, M470L3, Thorlabs) and a violet
734 LED (405 nm, M405L3, Thorlabs) with a 405 nm excitation filter (#65-133, Edmund optics). The
735 excitation light was collimated using adjustable collimator lenses (SM2E, Thorlabs). Using a dichroic
736 mirror (no. 87–063, Edmund optics), both excitation light paths were merged and then reflected onto
737 the brain surface using a second dichroic mirror (495 nm long-pass, T495lpxr, Chroma). GCaMP6s
738 fluorescence signals were isolated using a 525 nm emission filter (86-963, Edmund optics) in front of
739 the camera. Images acquired under violet illumination captured calcium-independent fluorescence at
740 the isosbestic point of GCaMP[99]. Therefore, by subtracting the linearly-rescaled calcium-independent
741 signal from the calcium-dependent signal acquired under blue illumination, we could remove the intrinsic
742 signal due to hemodynamic fluctuations.

743 Widefield imaging data were motion corrected using a subpixel image registration routine[100] was
744 performed separately for frames acquired under blue or violet illumination. Then, a singular value
745 decomposition (SVD) was used to reduce the dimensionality of the data and computational cost
746 associated with the analysis[101]. All subsequent analysis across time was performed on the 500
747 components that described the highest variance in the imaging data. Furthermore, a zero-phase,
748 second-order Butterworth filter was used to remove slow signal drifts below 0.1 Hz before performing
749 the hemodynamic correction. All subsequent analyses were based on this low-dimensional and
750 hemodynamic-corrected signal.

751 All recordings were aligned to the Allen CCF based on anatomical landmarks, and the location of V1
752 and higher visual areas (HVAs) was additionally confirmed using retinotopic mapping as described
753 above[49,53]. Due to the faster neural signals with GCaMP-related widefield imaging, we used a faster

754 movement of the bar aperture (2 s instead of 18 s per period with 20 repetitions for each direction). The
755 same retinotopic mapping procedure was also used for mice in the two-photon and electrophysiology
756 experiments, where the imaging was done through the cranial window (Fig. S14a).

757 **Electrophysiological recordings.** Electrophysiological recordings were done with Neuropixels 1.0
758 Probes[55] in head-fixed awake mice freely running on a wheel. For each mouse, we performed four
759 recordings on subsequent days. To later recover the probe position in each recording, the probes were
760 painted with DiD cell labeling solution (Invitrogen V22887) before each recording. To record neural
761 responses to motion cloud stimuli across all cortical layers, we targeted the center of V1 (4 mm posterior
762 and 2.5 mm lateral from bregma) and inserted the probe perpendicular to the cortical surface (6
763 recordings in 3 mice) to a depth of 2 mm. To simultaneously record from V1 and SC, the probes were
764 angled to 35° elevation and inserted to a depth of 3.6 mm. Neuropixels were positioned with a high-
765 precision micromanipulator (uMp-4, Sensapex) at a speed of 10 µm/s. In each recording, the insertion
766 point was moved by ~100 um in either mediolaterally or rostral-caudal direction from the target
767 coordinate to ensure that fluorescent electrode tracts could be later related to the probe position in
768 individual recording sessions (Fig. S11a and S14b). To determine the surface of the SC, we took
769 advantage of the visible gap in visual responses between the cortex and SC and determined the SC
770 surface at the depth at which we could detect visual LFPs after this gap. In agreement with our
771 histological results, this was usually at a depth of 1.63±0.16 mm.

772 All visual stimuli were presented at a 17 cm distance from the right eye on a gamma-corrected LED-
773 backlit LCD monitor (Viewsonic VX3276-2K-MHD-2, 32", 60Hz refresh rate). Similar to the two-photon
774 experiments, we then presented visual stimuli from the orientation band expanding and spatial
775 frequency band expanding protocols (see 'Visual stimulation' section below). Data acquisition from the
776 Neuropixels probe was done using SpikeGLX v3.6 (https://github.com/billkarsh/SpikeGLX, Bill Karsh).
777 High-pass filtered signals were recorded from 384 channels at 30 kHz, and low-pass filtered signals
778 were recorded at 2.5 kHz. The data was then time-shifted and median-subtracted with CatGT 3.9.
779 Channels that were broken or outside the brain were detected using SpikeInterface[102] and removed
780 from further analysis. The data was then spike-sorted with Kilosort 2.5 and manually curated using phy
781 2.0b1 (https://github.com/kwikteam/phy). The criteria for manual curation were consistent spike
782 waveforms across at least three recording channels, stable spike amplitudes across the recording, and
783 a visible gap in the center of the auto-correlogram. In addition, we imposed a cutoff for neurons with
784 inter-spike-violations above 0.5, using the contamination rate method[103]. Sorted data were analyzed
785 using custom MATLAB code.

786 After all electrophysiological recordings were complete, the mice were first perfused with cooled PBS
787 and subsequently with 10% formalin. After storing the brains in sucrose solution with increasing
788 concentration from 10-30%, 50 µm-wide brain slices were cut using a Cryostat (CM3050 S, Leica).
789 Images of the brain slices were made using a fluorescent microscope (BZ x810, Keyence, Germany).

790 **Visual stimulation.** Motion cloud stimuli were generated using the Motion Cloud Package[42] and
791 adapted for display via custom MATLAB code (MATLAB R2019b, MathWorks). The package follows a

792 linear generative model for creating a dense mixing of localized moving gratings with random positions
793 based on predefined parameters. To ensure that neural responses were not strongly driven by the
794 individual properties of these random phase motion textures, 10 renderings (300 frames each) of each
795 stimulus were generated for each parameter combination. 20 repetitions of each rendering were then
796 presented in a pseudorandom sequence movie where stimulus presentation order was shuffled with a
797 restriction that prevents consecutive presentation of the same stimulus category. Motion cloud stimuli
798 were either enriched in orientation bandwidth (narrow: 5°, mid: 22.5°, broad: 45°; around a central
799 orientation of 0°; see also Fig. 1) or in spatial frequency bandwidth (narrow: 0.004 cpd, mid: 0.04 cpd,
800 broad: 0.4 cpd; around a central spatial frequency of 0.04 cpd; see also Fig. 2). To test the discrimination
801 of different central orientations or spatial frequencies (Fig. 6, 7) the central orientation was either 0° or
802 90° and the central spatial frequency either 0.04 cpd or 0.16 cpd. All motion clouds were presented on
803 the screen, drifting from nasal to temporal (or orthogonal to the central orientation) with a temporal
804 frequency of 1 Hz. For the orientation and spatial frequency bandwidth protocols, the stimulus duration
805 was 5 seconds, followed by a 5-second inter-stimulus interval during which a mean gray screen was
806 shown. An overview of all parameter combinations and protocols is shown in Table 1. To combine
807 changes in both orientation and spatial frequency bandwidth (Fig. 4, 5; 'mixed' condition), we used
808 motion cloud stimuli with a central spatial frequency of 0.04 cpd, a central orientation of 0° and a
809 temporal frequency of 1 Hz, and then increased the bandwidth of either spatial frequency, orientation
810 or both. The 'narrow' case consisted of 0.004 cpd spatial frequency bandwidth and 5° orientation
811 bandwidth and served as the baseline for the narrow bandwidth of both features. In the 'SF' case, the
812 spatial frequency was increased to 0.4 cpd while the orientation bandwidth remained at 5°. In the 'ORI'
813 case, the spatial frequency bandwidth remained at 0.004 cpd, and the orientation bandwidth was
814 increased to 45°. Lastly, in the 'mixed' condition, both spatial frequency and orientation bandwidth were
815 increased to 0.4 cpd and 45°, respectively. For each stimulus condition, we generated eight separate
816 stimulus renderings to reduce the risk of over-emphasizing neural responses to complex features that
817 could occur in a specific rendering. Each rendering had a total of 7 presentations as full-field stimulus
818 (56 presentations for each full-field stimulus).
819 To test for the impact of center surround suppression, we first used sparse noise stimulation to identify
820 the receptive field locations of the neurons in each recording session. The stimulus in each frame was
821 composed of four non-adjacent 12°x12° white squares over a black background[97]. The grouping of the
822 squares was pseudo-randomized to ensure that each location would be presented 20 times in total.
823 Each presentation lasted for 250 ms with an inter-stimulus interval of 750 ms. For each field of view,
824 we then performed an imaging session with sparse noise stimuli to identify the receptive fields (RF) of
825 all imaged neurons (see section 'Data analysis and statistics'). After the imaging session, we then
826 created a new stimulus set where all motion clouds were covered by a gray mask, and a circular, 15°
827 transparent aperture was placed in the center of the mean RF of the imaged population (Fig. 4b, 'Center
828 RF,' see also Fig. S6). In a second recording session, we then returned to the same field of view (based
829 on the vessel pattern and visually comparing the location of the imaged cortical neurons) and repeated
830 the sparse noise stimulation. Subsequently, we presented the full-field and center RF stimuli for the
831 narrow, SF, ORI, and mixed conditions, as described above. For both the full-field and center RF

conditions, we presented 56 stimuli, respectively, in pseudo-randomized order. The stimulus duration was 2 s, followed by a 4 s gray screen.

To test for orientation tuning (Fig. 4), we showed full-field drifting square wave gratings at five different orientations (-45°, 22.5°,0°, 25°, 45°; 0.04 cpd spatial frequency; 1 Hz temporal frequency) in pseudo-randomized order. The stimulus duration was 1 s, followed by a 2 s inter-stimulus interval where a gray screen was shown, and each stimulus was repeated 20 times.

Touchscreen chamber experiments. Behavioral experiments were performed in a custom-built operant conditioning touchscreen chamber, using a 10” screen for visual stimulation (Elo Touch 1002L monitor, running at 60Hz)[90]. All animals performed the experiments under a water restriction regime and received at least 1.5 ml of water per day to maintain their general well-being. They received water *ad libitum* on the weekends and had access to food *ad libitum* throughout the experiment. All mice were weighed daily and monitored before and during the behavioral experiments. In the first phases of pre-training, the animals were habituated to the touch screen chamber and learned to associate a green light with the availability of a reward. After the animals were able to collect at least one reward per minute, they proceeded to the next phase, where they had to first touch the screen to receive a reward, which was still indicated by a green light. Again, after the animals performed the sequence of touching the screen and collecting a reward at least once a minute, they were moved to a more specific training regime to perform either the orientation or spatial frequency discrimination task. All trained mice passed the initial criteria and could be trained on the discrimination tasks (see Supplementary Movie 5).

The *orientation discrimination task* started with the training for easy discrimination, where the animals had to discriminate a horizontal (target) from a vertical (distractor) sine-wave grating with a spatial frequency of 0.04 cpd. Each stimulus was shown through a circular aperture with a diameter of 7.5 cm, and stimuli were presented left and right from the screen center, with a distance of 10 cm between the stimulus and the screen center. After the animals reached a performance of at least 80% correct responses, we proceeded with a staircase procedure. In this staircase procedure, the difficulty level was dynamic. Every correct response was followed by a decrease in orientation difference of 3°, while an incorrect response was followed by an increase in orientation difference of 8°, leading to a target performance of 72.7%. After the animals could perform the staircase procedure, we obtained one orientation discrimination threshold per session, revealing the minimal orientation difference between the target and distractor stimulus that was required for robust task performance. In randomized sessions, motion clouds with different spatial frequency bandwidths were used. Only one spatial frequency bandwidth was used per session to test how the discrimination threshold would be affected by a given spatial frequency bandwidth. To later compare the perceptual impact of different spatial frequency bandwidths, all trials with an orientation difference between 40° and 50° were combined and averaged over all sessions.

The *spatial frequency discrimination task* followed a similar training regime. After the animals performed sufficiently in the pretraining (Fig. S15), they were trained to discriminate between two (0° central orientation) motion clouds of different spatial frequencies. Throughout pre-training, the animals had to discriminate different spatial frequency pairs (0.04 cpd vs 0.06, 0.12 or 0.16 cpd; Fig. S15). The animals

showed a stable discrimination between 0.04 and 0.16 cpd, after which different orientation bandwidths were introduced. The different orientation bandwidths were used within the same session because no adaptive staircase procedure was used in these experiments.

To ensure that animals did not develop an intrinsic side bias during the discrimination tasks, we used a bias correction routine[28]. In the initial ten trials, the position of the correct stimulus was randomized, and the bias correction was subsequently used to correct for direction and repetition bias. In case a bias was detected, the stimulus position was chosen to increase the probability of showing the target stimulus on the non-preferred side. If a repetition bias was detected, the probability of changing the target stimulus position from one trial to the next was increased. When no bias was detected, the position of the target and distractor stimulus was chosen randomly.

Data analysis and statistics. All data analysis was done in MATLAB (MATLAB R2022a, MathWorks).

Widefield. When computing V1 responses in the widefield, we first determined the 50% region of V1 that responded the strongest across all presented stimuli per mouse. This was needed to prevent obtaining artificially lower response magnitudes in V1 due to integrating too many pixels from medial V1 that showed much weaker visual responses. For Fig. 5c, V1 activity was averaged over this subregion of V1, and individual trial responses were pooled across mice.

Electrophysiology. To quantify the electrophysiological spiking responses of individual neurons to broadband stimulation (Fig. 5f-h), we computed the area under the receiver-operator characteristic curve (AUC) between the baseline and the stimulus period. This allows us to obtain a measure of how reliably a given neuron responded to each stimulus, regardless of its overall firing rates. As with the two-photon data, we first computed the mean firing rate during the stimulus and a 1-second baseline period for each stimulus presentation. To identify stimulus-responsive neurons, we then used a one-sided Mann-Whitney-U test to assess if the mean firing rate across all stimulus presentations was significantly larger than zero (p-value <0.05). For all stimulus-responsive neurons, we then computed the AUC between the baseline and stimulus periods to quantify how reliably they responded to each stimulus condition. An AUC of 1 indicates a perfect separation of the activity in the baseline and the stimulus period, and an AUC of 0.5 suggests complete overlap (see also Fig. S8).

Two-photon imaging. After each recording, two-photon imaging data were motion corrected, and individual neurons were isolated using the Suite2P package with model-based background subtraction[104]. Suite2p was used to perform rigid motion correction on the image stack, identify neurons, extract their fluorescence, and correct for neuropil contamination. ΔF/F traces for each neuron were then produced using the method of Jia et al.[105], skipping the final filtering step. To compute the stimulus-response amplitude (ΔF/F) of individual neurons in the two-photon data, we computed the median across all trials for the difference between the fluorescence during the first 2-3 seconds of the stimulus and a preceding 1-second-long baseline window for each stimulus presentation.

To identify neurons that were responsive to a specific visual stimulus, we used a one-sided Mann-Whitney-U test to assess if ΔF/F across all stimulus presentations was significantly larger than baseline (p-value < 0.05).

909 To identify the receptive field of neurons from the sparse noise paradigm, we also computed the ΔF/F
910 for each neuron to all sparse noise stimuli that contained a white square in a specific part of the screen.
911 This resulted in a set of neural responses for each 12° x 12° square on the screen, and we used a one-
912 sided Mann-Whitney-U test to identify significant responses to visual stimulation on a specific part of
913 the screen. For significantly responding neurons, we then inferred the center of the receptive field as
914 the stimulus location that resulted in the strongest neural responses.

915 We used DeepLabCut[106] V2.3.9 to analyze the pupil position (see Fig. S6). Eight reference points
916 around the lids and one pint at the center of the pupil were labeled and tracked. We binned the pupil
917 movement range area (4 pixels/bin) and then calculated the mean frequency at which the center was
918 located within a bin during the stimulus period.

919 To compute the orientation tuning for different neurons, we computed the ΔF/F in response to different
920 grating orientations and used a one-sided Mann-Whitney-U test to identify neurons that significantly
921 responded to any grating stimulus. Besides this, we did a linear interpolation of the tuning curves and
922 inferred the preferred grating orientation of responsive neurons as the orientation that induced the
923 strongest neural response. Only neurons with a clear orientation tuning, i.e., a difference between peaks
924 and troughs above the median of the peak and trough distribution of the whole population, were selected
925 for the multiple regressor model (Fig. 4h, i).

926 *Statistics.* Throughout the results section, we have reported mean ± s.e.m. When reporting the
927 normalized responding cell count for each stimulus per session, we normalized the cell count per
928 session by the number of neurons that responded to the lowest respective bandwidth. We then pooled
929 the cell counts from all recordings to test for significant differences in the number of responsive cells for
930 different feature bandwidths. Since recordings from the same animals are not fully independent
931 variables, we used a linear mixed-effects (LME) model (using the fitlme function in MATLAB) to
932 determine significant differences between groups wherever possible (normally distributed data). Here,
933 we included the stimulus and animal identity for the fixed and random effect coefficients, respectively.
934 This allowed us to test if the stimulus identity significantly explains differences between two stimulus
935 conditions while controlling for potential differences between animals. To test for significance, we
936 performed a likelihood ratio test between a mixed-effects model that only contained animal identity
937 versus a full mixed-effect model that contained both stimulus and animal identity. The reported p values
938 and T statistics, therefore, indicate whether the addition of the stimulus regressor added significant
939 information beyond the animal identity to explain differences between the tested conditions. We used
940 this approach to test for significant differences whenever samples (individual neurons or recordings)
941 were pooled across multiple animals (Fig. 1e; Fig. 2e; Fig. 3b-e; Fig. 5c-h; Fig. 6b-d, f-h). Additionally,
942 for testing the effect of orientation tuning versus surround modulation in Fig 4 g-i, we upgraded the
943 model to a multiple-regressor linear mixed effect model, whereby the orientation tuning, the center
944 response, and the surround modulation effect were used as regressors to determine the impact of each
945 regressor on the resulting changes.

946 The LME model formula was:

$$\mathrm{Rm}\,ij = \beta 0 + \beta 1\,\mathrm{Sm}ij + \beta 2\,\mathrm{Ot}ij + \beta 3\,\mathrm{Cr}ij + \mathrm{u}j + \epsilon ij \tag{1}$$

where Rm_{ij} is the response modulation for the *i*th observation within the *j*th animal, β_0 is the fixed intercept (the total mean response modulation across all animals and conditions), β_1 β_2 and β_3 are the fixed effect coefficients for the predictors: Sm (Surround modulation), Ot (Orientation tuning) and Cr (Center response). u_j is the random intercept for the *j*th animal, accounting for the variation between different animals, and ϵ_{ij} is the residual error term for the *i*th observation within the *j*th animal, which accounts for the variability not explained by the fixed effects or the random intercepts.

In cases where using the LME model for statistics was not possible due to the data being not normally distributed, such as for ΔF/F amplitudes of pooled cells (Fig. 1f-h; Fig. 2f-h; Fig. 4d-f; Fig. 7c-f), we used a Wilcoxon signed rank test and additionally did a mouse-wise comparison in Fig. S1.

If multiple comparisons were performed, for example, when comparing the number of responsive cells in the mid and broad-bandwidth to the narrow-band condition (Fig. 1e), we performed a Bonferroni-correction for the number of performed tests to adjust for a multiple-comparison bias. Here, we adjusted the α level to reach significance to α = 0.05 / n, where n was the number of performed tests. In the above example, two tests were performed, so a significant difference required a p-value below α = 0.05 / n = 0.025.

To further test if individual neurons selectively responded to the narrow-, mid-, or broad-range of either the orientation or spatial frequency bandwidth (Fig.S1d, h), we computed a bandwidth selectivity index BW_SI that was computed as the response difference to a given bandwidth (e.g., narrow-range, *Rn*) and the mean of the other two (e.g., mid- and broad-range, *Rm* and *Rb*), normalized by their sum.

$$BW_SI = \frac{Rn - \mathrm{mean}(Rm, Rb)}{Rn + \mathrm{mean}(Rm, Rb)} \tag{2}$$

The BW_SI is bounded between -1 and 1, with values > 0 indicating selectivity for a given bandwidth, such as the narrow range, while negative values indicate selectively weaker responses to that bandwidth. To test if the BW_SI for a given neuron could not be observed by chance, we performed a shuffle control. Here, we shuffled the labels for three bandwidth conditions and then re-computed the BW_SI to obtain a measure of possible BW_SI values that can occur due to random response fluctuations. For each neuron, we computed 1000 shuffled BW_SIs to obtain a random distribution and then tested if the real BW-SI was above the 95th percentile of the shuffle distribution. Neurons for which this was the case were counted as selectively responding to narrow, mid, or broad-range stimuli (outer paddle of the Euler diagrams in Fig.S1d, h). Neurons with negative BW_SI below the 5th percentile were counted as being mixed selective for the two bandwidths aside from the non-preferred bandwidth. For example, a neuron with a negative BW_SI below the shuffle control for the narrow-range bandwidth was counted as being selective for both the mid- and broad-range bandwidths (overlapping paddles of the Euler diagrams in Fig.1d, h). Lastly, neurons without any selectivity beyond the shuffle control were counted as non-bandwidth-selective (the center region of the Euler diagrams in Fig.S1d, h).

Using the same approach, we computed an orientation modulation index OMI to quantify the difference in neural responses to broad versus narrow feature bandwidth (Fig. 6c, g).

$$OMI = \frac{R_{broad} - R_{narrow}}{R_{broad} + R_{narrow}} \tag{3}$$

where R_{broad} and R_{narrow} are mean responses to broad- and narrowband stimuli, respectively. The OMI is bounded between -1 and 1, with positive values indicating increased responses to broadband stimulation and negative values indicating reduced responses to broadband stimulation.

To determine the ability of each neuron to discriminate between the two different central spatial frequencies or between two central orientations, we also computed the AUC between these stimulus conditions (Fig. 6c, g). We computed the median response amplitude to all stimulus presentations for a given central feature (0.04 versus 0.16 cpd for spatial frequency and 0° versus 90° for orientation) and computed the AUC as a normalized measure of response discriminability. Here, we used the absolute AUC as a measure of discriminability, regardless of the response preference for a given stimulus feature for a given neuron. This was done by computing the absolute AUC as

$$AUC_{abs} = |AUC - 0.5| * 2 \tag{4}$$

AUC_{abs} is bound between 0 and 1, with positive values indicating increased discriminability of neural responses between the two stimulus conditions. This is referred to as spatial frequency or orientation discrimination index in the Results section.

Visualization. All data figures were generated in MATLAB (MATLAB R2022a, MathWorks). Raincloud plots were generated with the Raincloud tool[107], and figures (Figures 1c, 2c, 3a, 4a, d, 5a, 7a, S4c, d, g, h, S9a) were created in BioRender[108]. For better visualization of the raincloud plots, outlier elements above or below3 median absolute deviations were excluded from the plots using the *rmoutliers* function in MATLAB. All values were included in the statistical analyses. Stars mark p-value ranges, whereby one to three stars respectively signify p-values smaller than 0.05, 0.01, and 0.001. If multiple tests were performed, significance thresholds were corrected for the number of comparisons (e.g., 0.05/n for one star).

Statistical analysis of natural images and motion cloud stimuli.

Orientation distribution analysis. The ImageJ[109] Directionality[110] plugin was used on a library[47] of nature photos (Fig. 1a, n = 1077 images) or a complete rendering of the motion cloud stimuli (Fig. 1b, n = 300 frames) to derive the distribution of directional changes in color intensity within a local gradient (5x5 Sobel filter is applied). Each image was loaded individually, and 180 bins of 1° each (range 1° - 180°) were selected. For each image, a data table of measured orientation contents in the given bin of orientations was saved. Finally, we calculated the mean and s.e.m. across all the individual images and plotted the respective curves (a light Gaussian fit, σ = 2 was applied) via custom MATLAB (MATLAB R2022a, MathWorks) scripts.

Spatial frequency spectrum analysis. We analyzed the distribution of spatial frequencies for a set of images from either a library of nature photos[47] (Fig. 2a, n = 1077 images) or a complete rendering of the motion cloud stimuli (Fig. 2b, n = 300 frames). Here, we computed the 2D FFT spectrum for each image individually. To describe the spatial frequency content of images independent of their orientation, we shifted the zero-frequency component to the center and averaged energies in the frequency domain depending on their Euclidian distance to the zero frequency. Units of the spatial frequency spectra were converted from cycles per image to cpd based on their presentation or acquisition. For motion cloud stimuli, we computed their angular size based on their presentation:

$$angular\ size\ =\ 2\ x\ arctan\left(\frac{monitor\ width}{2\ x\ distance\ to\ the\ eye}\right) \tag{5}$$

For the natural images, the angular size was derived based on the individual camera field angle of view of each album:

$$FOV\ =\ 2\ x\ arctan\left(\frac{sensor\ dimension}{2\ x\ crop\ factor\ x\ focal\ length}\right) \tag{6}$$

Finally, we calculated the mean and s.e.m. across all individual images and plotted the respective spectra.

Stimulus predictability analysis. Spatial autocorrelations were computed for individual stimulus frames using the analysis provided by (Portilla and Simoncelli, 2000)[16]. For the use of the Portilla-Simoncelli (PS) analysis, stimulus frames were cropped to a size of 256 by 512 pixels and spatially down-sampled by a factor of 2. Raw coefficient correlations presented in Fig. 4c were computed as the central sample of the real autocorrelation for a spatial neighborhood of 51 pixels. Maps of spatial autocorrelations were averaged over all frames in the stimulus library of a given condition and presented with the corresponding colormaps.

Stimulus separability. To estimate how variable different realizations of the same stimulus condition are, we performed a principal component analysis across all texture parameters generated by the PS analysis (including pixelStats, pixelLPStats, autoCorrReal, autoCorrMag, magMeans, cousinMagCorr, parentMagCorr, cousinRealCorr, parentRealCorr, varianceHPR). We computed the principal components for individual frames and then averaged coefficients across frames within individual stimulus realizations. This resulted in average coefficients for each of the eight realizations per stimulus condition, of which we present a projection onto the first two principal components (Fig. S7a).

Coefficient magnitude statistics. We investigated if expanding orientation- and SF bandwidths result in the emergence of higher-order structures in the stimuli by computing the cross-orientation- and cross-scale energies[16,18] (Fig. S7b, c). For this purpose, we computed the PS analysis using four orientations over six spatial scales for the steerable image pyramid decomposition. Cross-orientation energies are based on the “cousinMagCorr” parameter of the PS analysis, representing the correlations between

sub-band magnitudes of different orientations within the same spatial scale[16]. Here, we computed the average cross-orientation energy on the coarsest spatial scale between the 0° and the ±45° sub-band magnitudes, as these represent the dominant features in our stimuli. Cross-scale energies, given by the "parentMagCorr" parameter of the PS analysis, represent correlations of sub-band magnitudes with those of all orientations at the next coarser spatial scale[16]. Here, we focused on the cross-scale energy of the 0° magnitude sub-band of the steerable image pyramid between the two coarsest spatial scales. For both cross-energy measures, we tested for statistical differences between the stimulus conditions, using pair-wise Wilcoxon–Mann–Whitney U tests with subsequent Bonferroni correction, comparing energies across stimulus realizations. For this, we averaged cross energies over frames belonging to the same stimulus realization. For visualization purposes, we displayed the cross energies of individual stimulus frames after removing outliers.

Model for neural responses of V1 neurons. To explore if the increased neural responses and recruitment for larger orientation bandwidth stimuli can be explained by different orientation tuning of V1 neurons, we created a simple bank of Gabor filters model. To predict neuronal responses, we compute the response magnitude of individual Gabor filters using the imgaborfilt-function in MATLAB (MATLAB R2022a, MathWorks). The response magnitude of complex Gabor filter kernels represents the response of an ideal-phase filter; the model, therefore, assumes a uniform distribution of phase representation in V1. We also designed the bank of Gabors to match the known tuning properties of mouse V1. For this, all Gabor filters were generated with a spatial frequency bandwidth of 2.38 octaves, matching previous reports[38,50]. Further, we adjusted the spatial aspect ratio of the Gabor filters, determining the envelope ellipticity of the filter kernels, thereby affecting the orientation tuning width of a given filter. We estimated this parameter for Gabor filters with a spatial frequency of 0.04 cpd, presented with a corresponding full contrast, 0.04 cpd sine wave grating. To match the tuning width of ~22° half-width half-maximum previously reported for mouse V1 neurons[38,50], we used Gabor filters with a spatial aspect ratio of 0.55 (Fig. S3b). This represents an elongation of the supporting envelope in the direction of the parallel stripes of the filter. Furthermore, to capture a broad range of responses, we used Gabor filters tuned to 5 different spatial frequencies (0.01 cpd, 0.02 cpd, 0.04 cpd, 0.06 cpd, 0.08 cpd; Fig. S3c) within the predominantly represented range of spatial frequencies of mouse V1[2]. For each spatial frequency, we used filter kernels with 180 different orientations in 1° increments, resulting in a bank of 900 individual complex Gabor filter kernels that covered the full range of orientations. To compare and combine responses across Gabor filters with different spatial frequencies, we normalized Gabor filter responses to their optimal stimulus (a full contrast sine-wave grating of matching spatial frequency and orientation).

We then simulated V1 population responses to our motion cloud stimuli. To reduce the computational cost, we spatially downsampled stimulus frames by a factor of 4 and computed Gabor filter responses for each individual "location" within the central 30° by 30° patch (Fig. S4) around the stimulus center (37x37 sites in total) in the following denoted as such:

$$m(o, f, b, x, y) \mid o \in O, f \in F, b \in B, x \in X, y \in Y$$

$$O = (\{-45\,°, -22.5°, 0°, 22.5°, 45°\}; n_O = 5),$$
$$F = (\{0.01\ cpd, 0.02\ cpd, 0.04\ cpd, 0.06\ cpd, 0.08\ cpd\}; n_F = 5)$$
$$B = (\{narrow\ orientation\ bandwidth, broad\ orientation\ bandwidth\}; n_B = 2)$$
$$X = Y = \{1,2, \dots ,37\}$$

(7)

Here, m represents the response magnitude of a Gabor filter with orientation tuning o and spatial frequency tuning f in response to a stimulus with orientation bandwidth b at the location (x, y) within the center of the stimulus frame. x and y denote indices of the 37x37 grid of locations corresponding to the 30° x 30° patch around the stimulus center. Subsequent model fits were generated based on the response at the stimulus center, either on its own or modulated by the average surrounding filter responses (Fig. 3, Fig. S3, and Fig. S4). The Gabor responses at the stimulus center were obtained using the center position and averaging over the 5 Gabors with different spatial frequency tuning:

$$c(o, b) = \frac{1}{n_F} \sum_{f \in F}^{n_F} m(o, f, b, x_c, y_c)$$

(8)

To translate these normalized Gabor filter response magnitudes into ΔF/F values that matched the measured neuronal response amplitudes, we computed a scaling factor w_t (Fig. S4). To determine this factor, we first measured the median responses of V1 neurons with different orientation tuning to narrow and ORI stimuli (-45 °, -22.5°, 0°, 22.5°, 45°; Figure 3b, c) and then calculated the mean across all bins to equally weigh responses from differently tuned neurons. The average neural response amplitude was 1.622% ΔF/F. Second, we selected response magnitudes from Gabor filters with matching orientation tuning contained in set O and averaged responses across filters with these five orientation tunings, five spatial frequencies, and across stimulus conditions. This yielded an average normalized Gabor response magnitude of 0.1627 arbitrary units. From these two measures, we then derived the scaling factor:

$$w_t = \frac{1}{n_O n_B} \times \frac{\sum_{b \in B}^{n_B} \left(\sum_{o \in O}^{n_O} a(o, b) \right)}{\sum_{b \in B}^{n_B} \left(\sum_{o \in O}^{n_O} c(o, b) \right)} = \frac{0.01622\ \Delta F/F}{0.1627\ AU.} = 0.0997$$

(9)

Here, w_t represents the scaling factor from Gabor response magnitudes to match the measured neural responses to different stimulus conditions, based on their orientation tuning (a (o, b); analogous to c (o, b)) in units of ΔF/F (Fig. 3b, c). We termed these scaled Gabor responses the “Tuning only model” as they are solely based on the scaled, orientation-dependent Gabor filter responses at the central stimulus location (Fig. 3b, c; Fig. S4). The tuning-only model responses were computed as follows:

$$tuning\ only\ responses(o, b) = w_t \times c(o, b)$$

(10)

The “Tuning only model” fit showed the strongest deviation from the experimental data in the narrow condition. Since narrow stimuli also have a more regular spatial structure compared to ORI stimuli (Figure 4c), we hypothesized that the difference between the modeled and experimental data could be explained by surround modulation. We, therefore, included an additional interaction between the center and spatially surrounding Gabor responses within the 30° by 30° patch into the model. This “Suppression model” used divisive surround suppression to normalize center responses:

$$suppression\ model\ responses(o,b) = \frac{1}{n_F}\sum_{f\,\epsilon\,F}^{n_F}\frac{w_c \times m(o,f,b,x_c,y_c)}{1 + w_s \times \max(0, s(o,f,b) + t)} \tag{11}$$

Here, w_c, w_s, and t represent fitted model parameters, and s was defined as the average response magnitude of Gabor filters with the same orientation and spatial frequency tuning as in the center but from the surround region.

$$s(o,f,b) = \frac{1}{|P|}\sum_{x,y\epsilon P}^{n=|P|} m(o,f,b,x,y) \tag{12}$$

With:

$$P = \{(x,y)|x \in X, y \in Y and\ d(x,y) > lim_i\ and\ d(x,y) < lim_o\}$$
$$d(x,y) = \sqrt{(x-x_c)^2 + (y-y_c)^2} \tag{13}$$

Here, P defines the set of “valid” 2D (x,y) coordinates within the 37 x 37 grid of Gabor responses that define the surround region. |P| denotes the cardinality of the set P. P depends on the model parameters lim_i and lim_o, which define the minimum and maximum distance from the center Gabor response to qualify as part of the surround (converted from degrees to corresponding units).

We then fitted the suppression model using these five parameters: the minimum and maximum distance from the center at which responses were considered as contributing to the surround modulation (lim_i, lim_o), the weight of the center and surround responses (w_c, w_s) and the surround response threshold (t). This surround suppression acted on the level of individual frame responses and was fit to the response over the entire stimulus dataset using the fminsearchbnd-function (John D'Errico, 2006; Matlab file-exchange). This allowed us to limit the surround region from 7.5° to 15° displacement from the central Gabor, as well as limit w_c and w_s to positive values. For the presented model, we used the parameters of the best fit over 100 individual model fits with random parameter initializations. The presented, best fitting model used the following parameters: lim_i= 11.19°, lim_o=12.19°, w_c=11.9, w_s=1295.1 and t=-0.2 arbitrary units. The resulting orientation-tuning dependent fit is shown in Fig. 3b, c. From these fitted narrow and ORI responses, we then derived the “response modulation” shown in Fig. 3d.

To generate a fit for the expected recruitment, based on the “tuning only model” as well as the “suppression model”, we used a simple linear regression without an intercept term to translate the fitted ORI response modulation to orientation-dependent neuronal recruitment (Fig. 3e). Our underlying assumption was that a higher response amplitude should be reflected in a higher fraction of neurons reaching the response criterion, resulting in larger recruitment. The fitted recruitment is derived from the Gabor response magnitude:

$$recruitment\ modulation(o) = \beta \times response\ modulation(o) \tag{14}$$

The fit for translating response to recruitment modulation was $\beta_{\text{tuning only model}}$=0.134 for the Tuning only model and $\beta_{\text{suppression model}}$=1.141 for the Suppression model. Lastly, we computed the mean-corrected coefficient of determination (R^2) to evaluate how well our models described orientation-dependent differences in the observed broadband response and recruitment modulation.

Data Availability

The processed data have been deposited in Zenodo [https://doi.org/10.5281/zenodo.14605878]. The natural image library[47] used for natural feature distribution analysis is accessible at [http://tofu.psych.upenn.edu/~upennidb]. Source data are provided with this paper.

Code Availability

Image analysis, data analysis as well as the Gabor filter bank models can be found in GitHub [https://github.com/AachenBrainLab/Eyes_Wide_Bandwidth].

References

1. Schwartz, O. & Simoncelli, E. P. Natural signal statistics and sensory gain control. *Nat. Neurosci.* **4**, 819–825 (2001).
2. Girshick, A. R., Landy, M. S. & Simoncelli, E. P. Cardinal rules: visual orientation perception reflects knowledge of environmental statistics. *Nat. Neurosci.* **14**, 926–932 (2011).
3. Simoncelli, E. P. Natural Image Statistics and Neural Representation. *Annu. Rev. Neurosci.* **24**, 1193–1216 (2001).
4. Barlow, H. B. Single Units and Sensation: A Neuron Doctrine for Perceptual Psychology? *Perception* **1**, 371–394 (1972).
5. Bányai, M. *et al.* Stimulus complexity shapes response correlations in primary visual cortex. *Proc. Natl. Acad. Sci.* **116**, 2723–2732 (2019).
6. Yu, Y., Stirman, J. N., Dorsett, C. R. & Smith, S. L. Selective representations of texture and motion in mouse higher visual areas. *Curr. Biol.* **32**, 2810-2820.e5 (2022).
7. Clark, D. A. *et al.* Flies and humans share a motion estimation strategy that exploits natural scene statistics. *Nat. Neurosci.* **17**, 296–303 (2014).
8. Stringer, C., Pachitariu, M., Steinmetz, N., Carandini, M. & Harris, K. D. High-dimensional geometry of population responses in visual cortex. *Nature* **571**, 361–365 (2019).
9. Walker, E. Y. *et al.* Inception loops discover what excites neurons most using deep predictive models. *Nat. Neurosci.* **22**, 2060–2065 (2019).
10. Kayser, C. Processing of complex stimuli and natural scenes in the visual cortex. *Curr. Opin. Neurobiol.* **14**, 468–473 (2004).
11. Stansbury, D. E., Naselaris, T. & Gallant, J. L. Natural Scene Statistics Account for the Representation of Scene Categories in Human Visual Cortex. *Neuron* **79**, 1025–1034 (2013).
12. Antolík, J., Hofer, S. B., Bednar, J. A. & Mrsic-Flogel, T. D. Model Constrained by Visual Hierarchy Improves Prediction of Neural Responses to Natural Scenes. *PLOS Comput. Biol.* **12**, e1004927 (2016).
13. Felsen, G. & Dan, Y. A natural approach to studying vision. *Nat. Neurosci.* **8**, 1643–1646 (2005).
14. Rust, N. C. & Movshon, J. A. In praise of artifice. *Nat. Neurosci.* **8**, 1647–1650 (2005).
15. Benda, J., Gollisch, T., Machens, C. K. & Herz, A. V. From response to stimulus: adaptive sampling in sensory physiology. *Curr. Opin. Neurobiol.* **17**, 430–436 (2007).

16. Portilla, J. & Simoncelli, E. P. A Parametric Texture Model Based on Joint Statistics of Complex Wavelet Coefficients. *Int. J. Comput. Vis.* **40**, 49–70 (2000).
17. Hermundstad, A. M. *et al.* Variance predicts salience in central sensory processing. *eLife* **3**, e03722 (2014).
18. Freeman, J., Ziemba, C. M., Heeger, D. J., Simoncelli, E. P. & Movshon, J. A. A functional and perceptual signature of the second visual area in primates. *Nat. Neurosci.* **16**, 974–981 (2013).
19. Okazawa, G., Tajima, S. & Komatsu, H. Image statistics underlying natural texture selectivity of neurons in macaque V4. *Proc. Natl. Acad. Sci.* **112**, (2015).
20. Bolaños, F. *et al.* Efficient coding of natural images in the mouse visual cortex. *Nat. Commun.* **15**, 2466 (2024).
21. Tesileanu, T., Piasini, E. & Balasubramanian, V. Efficient processing of natural scenes in visual cortex. *Front. Cell. Neurosci.* **16**, 1006703 (2022).
22. Samonds, J. M., Feese, B. D., Lee, T. S. & Kuhlman, S. J. Nonuniform surround suppression of visual responses in mouse V1. *J. Neurophysiol.* **118**, 3282–3292 (2017).
23. Bolz, J. & Gilbert, C. D. Generation of end-inhibition in the visual cortex via interlaminar connections. *Nature* **320**, 362–365 (1986).
24. Tkačik, G., Prentice, J. S., Victor, J. D. & Balasubramanian, V. Local statistics in natural scenes predict the saliency of synthetic textures. *Proc. Natl. Acad. Sci.* **107**, 18149–18154 (2010).
25. Victor, J. D., Conte, M. M. & Chubb, C. F. Textures as Probes of Visual Processing. *Annu. Rev. Vis. Sci.* **3**, 275–296 (2017).
26. Yu, Y., Schmid, A. M. & Victor, J. D. Visual processing of informative multipoint correlations arises primarily in V2. *eLife* **4**, e06604 (2015).
27. Caramellino, R. *et al.* Rat sensitivity to multipoint statistics is predicted by efficient coding of natural scenes. *eLife* **10**, e72081 (2021).
28. Wiesbrock, C., Musall, S. & Kampa, B. M. A flexible Python-based touchscreen chamber for operant conditioning reveals improved visual perception of cardinal orientations in mice. *Front. Cell. Neurosci.* **16**, 866109 (2022).
29. Roth, M. M., Helmchen, F. & Kampa, B. M. Distinct Functional Properties of Primary and Posteromedial Visual Area of Mouse Neocortex. *J. Neurosci.* **32**, 9716–9726 (2012).
30. Kirchberger, L. *et al.* The essential role of recurrent processing for figure-ground perception in mice. *Sci. Adv.* **7**, eabe1833 (2021).

31. Adesnik, H., Bruns, W., Taniguchi, H., Huang, Z. J. & Scanziani, M. A neural circuit for spatial summation in visual cortex. *Nature* **490**, 226–231 (2012).
32. Vinje, W. E. & Gallant, J. L. Sparse Coding and Decorrelation in Primary Visual Cortex During Natural Vision. *Science* **287**, 1273–1276 (2000).
33. Haider, B. *et al.* Synaptic and Network Mechanisms of Sparse and Reliable Visual Cortical Activity during Nonclassical Receptive Field Stimulation. *Neuron* **65**, 107–121 (2010).
34. Pecka, M., Han, Y., Sader, E. & Mrsic-Flogel, T. D. Experience-Dependent Specialization of Receptive Field Surround for Selective Coding of Natural Scenes. *Neuron* **84**, 457–469 (2014).
35. Williford, J. R. & Von Der Heydt, R. Figure-Ground Organization in Visual Cortex for Natural Scenes. *eneuro* **3**, ENEURO.0127-16.2016 (2016).
36. Keller, A. J. *et al.* A Disinhibitory Circuit for Contextual Modulation in Primary Visual Cortex. *Neuron* **108**, 1181-1193.e8 (2020).
37. Keller, A. J., Roth, M. M. & Scanziani, M. Feedback generates a second receptive field in neurons of the visual cortex. *Nature* **582**, 545–549 (2020).
38. Niell, C. M. & Stryker, M. P. Highly Selective Receptive Fields in Mouse Visual Cortex. *J. Neurosci.* **28**, 7520–7536 (2008).
39. Goris, R. L. T., Simoncelli, E. P. & Movshon, J. A. Origin and Function of Tuning Diversity in Macaque Visual Cortex. *Neuron* **88**, 819–831 (2015).
40. Han, X., Vermaercke, B. & Bonin, V. Diversity of spatiotemporal coding reveals specialized visual processing streams in the mouse cortex. *Nat. Commun.* **13**, 3249 (2022).
41. Niell, C. M. Cell Types, Circuits, and Receptive Fields in the Mouse Visual Cortex. *Annu. Rev. Neurosci.* **38**, 413–431 (2015).
42. Leon, P. S., Vanzetta, I., Masson, G. S. & Perrinet, L. U. Motion clouds: model-based stimulus synthesis of natural-like random textures for the study of motion perception. *J. Neurophysiol.* **107**, 3217–3226 (2012).
43. Bonin, V., Histed, M. H., Yurgenson, S. & Reid, R. C. Local Diversity and Fine-Scale Organization of Receptive Fields in Mouse Visual Cortex. *J. Neurosci.* **31**, 18506–18521 (2011).
44. Froudarakis, E. *et al.* Population code in mouse V1 facilitates readout of natural scenes through increased sparseness. *Nat. Neurosci.* **17**, 851–857 (2014).
45. Kampa, B. Representation of visual scenes by local neuronal populations in layer 2/3 of mouse visual cortex. *Front. Neural Circuits* **5**, (2011).

46. Ganguli, D. & Simoncelli, E. P. Implicit encoding of prior probabilities in optimal neural populations. *Adv Neural Inf Process Syst.* (2014).

47. Tkačik, G. *et al.* Natural Images from the Birthplace of the Human Eye. *PLoS ONE* **6**, e20409 (2011).

48. Andermann, M. L., Kerlin, A. M., Roumis, D. K., Glickfeld, L. L. & Reid, R. C. Functional Specialization of Mouse Higher Visual Cortical Areas. *Neuron* **72**, 1025–1039 (2011).

49. Marshel, J. H., Garrett, M. E., Nauhaus, I. & Callaway, E. M. Functional Specialization of Seven Mouse Visual Cortical Areas. *Neuron* **72**, 1040–1054 (2011).

50. Van Den Bergh, G., Zhang, B., Arckens, L. & Chino, Y. M. Receptive-field properties of V1 and V2 neurons in mice and macaque monkeys. *J. Comp. Neurol.* **518**, 2051–2070 (2010).

51. Wang, Q. *et al.* The Allen Mouse Brain Common Coordinate Framework: A 3D Reference Atlas. *Cell* **181**, 936-953.e20 (2020).

52. Garrett, M. E., Nauhaus, I., Marshel, J. H. & Callaway, E. M. Topography and Areal Organization of Mouse Visual Cortex. *J. Neurosci.* **34**, 12587–12600 (2014).

53. Zhuang, J. *et al.* An extended retinotopic map of mouse cortex. *eLife* **6**, e18372 (2017).

54. Kalatsky, V. A. & Stryker, M. P. New Paradigm for Optical Imaging. *Neuron* **38**, 529–545 (2003).

55. Jun, J. J. *et al.* Fully integrated silicon probes for high-density recording of neural activity. *Nature* **551**, 232–236 (2017).

56. Vaiceliunaite, A., Erisken, S., Franzen, F., Katzner, S. & Busse, L. Spatial integration in mouse primary visual cortex. *J. Neurophysiol.* **110**, 964–972 (2013).

57. Guo, K., Robertson, R. G., Mahmoodi, S. & Young, M. P. Centre-surround interactions in response to natural scene stimulation in the primary visual cortex. *Eur. J. Neurosci.* **21**, 536–548 (2005).

58. Coen-Cagli, R., Kohn, A. & Schwartz, O. Flexible gating of contextual influences in natural vision. *Nat. Neurosci.* **18**, 1648–1655 (2015).

59. Rao, R. P. N. & Ballard, D. H. Predictive coding in the visual cortex: a functional interpretation of some extra-classical receptive-field effects. *Nat. Neurosci.* **2**, 79–87 (1999).

60. Peters, A. J., Fabre, J. M. J., Steinmetz, N. A., Harris, K. D. & Carandini, M. Striatal activity topographically reflects cortical activity. *Nature* **591**, 420–425 (2021).

61. Zmarz, P. & Keller, G. B. Mismatch Receptive Fields in Mouse Visual Cortex. *Neuron* **92**, 766–772 (2016).

62. Keller, G. B., Bonhoeffer, T. & Hübener, M. Sensorimotor Mismatch Signals in Primary Visual Cortex of the Behaving Mouse. *Neuron* **74**, 809–815 (2012).

63. Fiser, A. *et al.* Experience-dependent spatial expectations in mouse visual cortex. *Nat. Neurosci.* **19**, 1658–1664 (2016).
64. Keller, G. B. & Mrsic-Flogel, T. D. Predictive Processing: A Canonical Cortical Computation. *Neuron* **100**, 424–435 (2018).
65. Gallimore, C. G., Ricci, D. & Hamm, J. P. Spatiotemporal dynamics across visual cortical laminae support a predictive coding framework for interpreting mismatch responses. Preprint at http://biorxiv.org/lookup/doi/10.1101/2023.04.17.537173 (2023).
66. Harris, K. D. & Mrsic-Flogel, T. D. Cortical connectivity and sensory coding. *Nature* **503**, 51–58 (2013).
67. Fu, J. *et al. Pattern Completion and Disruption Characterize Contextual Modulation in Mouse Visual Cortex*. http://biorxiv.org/lookup/doi/10.1101/2023.03.13.532473 (2023).
68. Vinje, W. E. & Gallant, J. L. Natural Stimulation of the Nonclassical Receptive Field Increases Information Transmission Efficiency in V1. *J. Neurosci.* **22**, 2904–2915 (2002).
69. Busse, L., Wade, A. R. & Carandini, M. Representation of Concurrent Stimuli by Population Activity in Visual Cortex. *Neuron* **64**, 931–942 (2009).
70. DeAngelis, G. C., Robson, J. G., Ohzawa, I. & Freeman, R. D. Organization of suppression in receptive fields of neurons in cat visual cortex. *J. Neurophysiol.* **68**, 144–163 (1992).
71. Freeman, T. C. B., Durand, S., Kiper, D. C. & Carandini, M. Suppression without Inhibition in Visual Cortex. *Neuron* **35**, 759–771 (2002).
72. Ringach, D. L. The geometry of masking in neural populations. *Nat. Commun.* **10**, 4879 (2019).
73. Ladret, H. J. *et al.* Cortical recurrence supports resilience to sensory variance in the primary visual cortex. *Commun. Biol.* **6**, 667 (2023).
74. Muir, D. R., Molina-Luna, P., Roth, M. M., Helmchen, F. & Kampa, B. M. Specific excitatory connectivity for feature integration in mouse primary visual cortex. *PLOS Comput. Biol.* **13**, e1005888 (2017).
75. Palagina, G., Meyer, J. F. & Smirnakis, S. M. Complex Visual Motion Representation in Mouse Area V1. *J. Neurosci.* **37**, 164–183 (2017).
76. Barbera, D., Priebe, N. J. & Glickfeld, L. L. Feedforward mechanisms of cross-orientation interactions in mouse V1. *Neuron* **110**, 297-311.e4 (2022).
77. Ruderman, D. L. & Bialek, W. Statistics of natural images: Scaling in the woods. *Phys. Rev. Lett.* **73**, 814–817 (1994).

78. Guan, S.-C., Zhang, S.-H., Zhang, Y.-C., Tang, S.-M. & Yu, C. Plaid Detectors in Macaque V1 Revealed by Two-Photon Calcium Imaging. *Curr. Biol.* **30**, 934-940.e3 (2020).
79. Juavinett, A. L. & Callaway, E. M. Pattern and Component Motion Responses in Mouse Visual Cortical Areas. *Curr. Biol.* **25**, 1759–1764 (2015).
80. Muir, D. R., Roth, M. M., Helmchen, F. & Kampa, B. M. Model-based analysis of pattern motion processing in mouse primary visual cortex. *Front. Neural Circuits* **9**, (2015).
81. Simoncini, C., Perrinet, L. U., Montagnini, A., Mamassian, P. & Masson, G. S. More is not always better: adaptive gain control explains dissociation between perception and action. *Nat. Neurosci.* **15**, 1596–1603 (2012).
82. Gao, E., DeAngelis, G. C. & Burkhalter, A. Parallel Input Channels to Mouse Primary Visual Cortex. *J. Neurosci.* **30**, 5912–5926 (2010).
83. Dyballa, L., Hoseini, M. S., Dadarlat, M. C., Zucker, S. W. & Stryker, M. P. Flow stimuli reveal ecologically appropriate responses in mouse visual cortex. *Proc. Natl. Acad. Sci.* **115**, 11304–11309 (2018).
84. Hasani, H., Soleymani, M. & Aghajan, H. Surround Modulation: A Bio-inspired Connectivity Structure for Convolutional Neural Networks. in *Advances in Neural Information Processing Systems* (eds. Wallach, H. et al.) vol. 32 (Curran Associates, Inc., 2019).
85. Bergen, J. R. & Julesz, B. Rapid discrimination of visual patterns. *IEEE Trans. Syst. Man Cybern.* **SMC-13**, 857–863 (1983).
86. Lamme, V. The neurophysiology of figure-ground segregation in primary visual cortex. *J. Neurosci.* **15**, 1605–1615 (1995).
87. Treisman, A. M. & Gelade, G. A feature-integration theory of attention. *Cognit. Psychol.* **12**, 97–136 (1980).
88. Ahmadlou, M., Tafreshiha, A. & Heimel, J. A. Visual Cortex Limits Pop-Out in the Superior Colliculus of Awake Mice. *Cereb. Cortex* **27**, 5772–5783 (2017).
89. White, B. J. *et al.* Superior colliculus neurons encode a visual saliency map during free viewing of natural dynamic video. *Nat. Commun.* **8**, 14263 (2017).
90. Smith, A. T. & Edgar, G. K. The influence of spatial frequency on perceived temporal frequency and perceived speed. *Vision Res.* **30**, 1467–1474 (1990).
91. Felsen, G., Touryan, J., Han, F. & Dan, Y. Cortical Sensitivity to Visual Features in Natural Scenes. *PLoS Biol.* **3**, e342 (2005).

1357 92. Guo, Z. V. *et al.* Flow of Cortical Activity Underlying a Tactile Decision in Mice. *Neuron* **81**, 179–194
1358 (2014).
1359 93. Couto, J. *et al.* Chronic, cortex-wide imaging of specific cell populations during behavior. *Nat. Protoc.* **16**,
1360 3241–3263 (2021).
1361 94. Brainard, D. H. The Psychophysics Toolbox. *Spat. Vis.* **10**, 433–436 (1997).
1362 95. Pelli, D. G. The VideoToolbox software for visual psychophysics: transforming numbers into movies. *Spat.*
1363 *Vis.* **10**, 437–442 (1997).
1364 96. Pologruto, T. A., Sabatini, B. L. & Svoboda, K. ScanImage: Flexible software for operating laser scanning
1365 microscopes. *Biomed. Eng. OnLine* **2**, 13 (2003).
1366 97. Van Beest, E. H. *et al.* Mouse visual cortex contains a region of enhanced spatial resolution. *Nat. Commun.*
1367 **12**, 4029 (2021).
1368 98. Ratzlaff, E. H. & Grinvald, A. A tandem-lens epifluorescence macroscope: Hundred-fold brightness
1369 advantage for wide-field imaging. *J. Neurosci. Methods* **36**, 127–137 (1991).
1370 99. Lerner, T. N. *et al.* Intact-Brain Analyses Reveal Distinct Information Carried by SNc Dopamine
1371 Subcircuits. *Cell* **162**, 635–647 (2015).
1372 100. Guizar-Sicairos, M., Thurman, S. T. & Fienup, J. R. Efficient subpixel image registration algorithms.
1373 *Opt. Lett.* **33**, 156 (2008).
1374 101. Musall, S., Kaufman, M. T., Juavinett, A. L., Gluf, S. & Churchland, A. K. Single-trial neural
1375 dynamics are dominated by richly varied movements. *Nat. Neurosci.* **22**, 1677–1686 (2019).
1376 102. Buccino, A. P. *et al.* SpikeInterface, a unified framework for spike sorting. *eLife* **9**, e61834 (2020).
1377 103. Hill, D. N., Mehta, S. B. & Kleinfeld, D. Quality Metrics to Accompany Spike Sorting of Extracellular
1378 Signals. *J. Neurosci.* **31**, 8699–8705 (2011).
1379 104. Pachitariu, M. *et al.* Suite2p: beyond 10,000 neurons with standard two-photon microscopy. Preprint at
1380 http://biorxiv.org/lookup/doi/10.1101/061507 (2017).
1381 105. Jia, H., Rochefort, N. L., Chen, X. & Konnerth, A. In vivo two-photon imaging of sensory-evoked
1382 dendritic calcium signals in cortical neurons. *Nat. Protoc.* **6**, 28–35 (2011).
1383 106. Mathis, A. *et al.* DeepLabCut: markerless pose estimation of user-defined body parts with deep
1384 learning. *Nat. Neurosci.* **21**, 1281–1289 (2018).
1385 107. Allen, M. *et al.* Raincloud plots: a multi-platform tool for robust data visualization. *Wellcome Open*
1386 *Res.* **4**, 63 (2021).

108. Created in BioRender. Balla, E. https://BioRender.com/g05l789 (2025).

109. Schneider, C. A., Rasband, W. S. & Eliceiri, K. W. NIH Image to ImageJ: 25 years of image analysis. *Nat. Methods* **9**, 671–675 (2012).

110. Liu, Z.-Q. Scale space approach to directional analysis of images. *Appl. Opt.* **30**, 1369 (1991).

Acknowledgments

We would like to thank Laurent Perrinet, Hugo Ladret, Ivo Vanzetta, and Frédéric Chavanne for helpful insights on the motion cloud stimuli and fruitful discussions on the project and manuscript; Magdalena Robacha for help with the mouse preparation and imaging, Fatemeh Yousefi for help with the pupil tracking. This work was supported by the Deutsche Forschungsgemeinschaft (DFG, German Research Foundation) - 368482240/GRK2416 (B.K.) and 430156848/SPP2205 (B.K.), the Helmholtz association VH-NG-1611 (S.M.) and the state of North Rhine-Westphalia through the iBehave initiative (B.K., S.M., E.B.)

Author contributions

B.M.K., C.W., and E.B. conceived and planned the experiments. E.B. designed the two-photon experiments, collected the neural data, and performed the analysis with input from B.M.K. and S.M. G.N. generated the stimuli, collected and analyzed the intrinsic- and widefield imaging data, and built the model of V1. C.W. and J.L. designed the 2AFC task, collected the behavioral data, and performed the analysis. S.G. and S.M. collected and analyzed the electrophysiological data. E.B. wrote the initial draft and generated the figures with input from B.M.K and S.M. The manuscript was revised and completed by B.M.K and S.M. All authors read and approved the final manuscript.

Competing Interests Statement

The authors declare no competing interests.

Tables

	Central Orientation (°)	Orientation bandwidth (°)	Central Spatial Frequency (cpd)	Spatial Frequency bandwidth (cpd)
Orientation band expanding	0	0, 25, 90	0.04, 0.16	0.004
Spatial frequency band expanding	0, 90	3	0.04	0.004, 0.04, 0.4

1415

1416 **Table 1. Specific Parameters for the orientation and spatial frequency band expanding protocols.** To
1417 investigate the effect of the orientation bandwidth band expanding (orientation band enrichment protocol, top row),
1418 the central orientation (first column) and spatial frequency bandwidth (last column) were kept constant (0° and
1419 0.04cpd, respectively), while different combinations of orientation bandwidth (second column: 5°, 25°, 45°) and
1420 central spatial frequency (third column: 0.04 cpd and 0.16 cpd) were presented. This resulted in a total of 6 different
1421 stimulus parameter combinations. The same principle was used for the spatial frequency band expanding protocol
1422 (bottom row).

1423

1424 ## Figure Legends/Captions

1425

1426 **Figure 1. V1 neurons are most responsive to broad orientation bandwidths.**
1427 (**a**) Mean orientation distributions from natural images (example images adapted from Tkacik G et al, "Natural
1428 images from the birthplace of the human eye ", PLoS ONE 6: e20409 (2011), n = 1077 images, shading shows
1429 s.e.m.). Single-cell selectivity was tested at specific orientations (dashed lines, Fig. 3, Fig. S2). Regions 1, 2 show
1430 mid-range or narrow orientation bandwidth examples. (**b**) Same as a) for broadband orientation bandwidth stimuli
1431 (5°, 25°, and 45°, n = 300 frames each). (**c**) Awake, head-fixed mice viewed differing orientation bandwidth stimuli
1432 while 2Photon-imaging V1 neural activity in layer 2/3. (**d**) Example session, showing V1 neural responses to
1433 different orientation bandwidths (5°, 25°, 45°, blue masks show responsive cells, scale bar: 100 µm, corresponding
1434 stimuli at top left). Traces show single-trial responses of four example cells with different orientation bandwidth
1435 preferences (scale bar: 1 s, 20% ΔF/F). (**e**) Counts of responsive neurons to each orientation bandwidth,
1436 normalized by the number of cells responding to the 5° bandwidth (n = 18 sessions from 9 mice). (**f**) Difference
1437 between mean response amplitude versus baseline for each orientation bandwidth. Shown are neurons with a
1438 significant response for at least one condition (1394 out of 4892 neurons, 29% ± 2% neurons per session; mean ±
1439 s.e.m.). Horizontal line shows the median narrow response amplitude. (**g**) Same as f) for neurons that consistently
1440 responded to all bandwidths (12% of responding cells per session, 252 total neurons). Horizontal line shows the
1441 median narrow response amplitude. (**h**) Same as f) for neurons that preferentially responded to narrow-band (left
1442 violin plots, 7% of responding cells per session, 152 in total), or to broadband (right violin plots, 23% of responding
1443 cells per session, 487 neurons in total). Box plots indicate median (horizonal line), interquartile range (box bounds:
1444 25th–75th percentiles), and whiskers (1.5× interquartile range). Dotted line is the narrow-band median. Stars mark
1445 significant (Bonferroni correction for two tests, α = 0.025) differences from two-sided tests against narrow condition:
1446 LME test (panel e) Wilcoxon signed rank (panels f, g) Wilcoxon ranked sum (panel h). Panel c was created in
1447 BioRender. Balla, E. https://BioRender.com/g05l789 (2025).

1448

1449 **Figure 2. V1 neurons are equally responsive to different spatial frequency bandwidths.**
1450 (**a**) Mean spatial frequency distributions from natural images (example images adapted from Tkacik G et al, "Natural
1451 images from the birthplace of the human eye ", PLoS ONE 6: e20409 (2011), n = 1077 images, shading shows
1452 s.e.m.). Single-cell selectivity was tested at specific spatial frequencies (dashed lines, Fig. S2). (**b**) Same as a) for
1453 broadband stimuli with different spatial frequency distributions (0.004 cpd, 0.04 cpd, and 0.4 cpd, n = 300 frames
1454 each). (**c**) Awake, head-fixed mice viewed differing orientation bandwidth stimuli while 2Photon-imaging V1 neural
1455 activity in layer 2/3. (**d**) Example session, showing V1 neural responses to different spatial frequency bandwidths
1456 (0.004 cpd, 0.04 cpd, 0.4 cpd, purple masks show responsive cells, scale bar: 100 µm, corresponding stimuli at
1457 top left). Traces show single-trial responses of 4 example cells with different spatial frequency bandwidth
1458 preferences (scale bar: 1 s, 20% ΔF/F). (**e**) Counts of responsive neurons to each spatial frequency bandwidth,
1459 normalized by the number of cells responding to 0.004 cpd bandwidth (n = 16 sessions). (**f**) Difference between
1460 mean response amplitude versus baseline for each orientation bandwidth. Shown are neurons with a significant
1461 response for at least one condition (603 of 3185 neurons, 19% ± 2% neurons per session; mean ± s.e.m.).
1462 Horizontal line shows the median narrow response amplitude. (**g**) Same as f) for neurons that consistently
1463 responded to all bandwidths (68 neurons, 9% of responding cells per session). Horizontal line shows the median
1464 narrow response amplitude. (**h**) Same as f) for neurons that preferentially responded to the narrow-band stimulus
1465 (left violin plots, 24% of responding cells per session, 133 in total), or the broadband stimulus (right violin plots,
1466 26% of responding cells per session, 132 neurons in total). Box plots indicate median (horizonal line), interquartile
1467 range (box bounds: 25th–75th percentiles), and whiskers (1.5× interquartile range). Dotted line is the narrow-band
1468 median. No significant (Bonferroni correction for two tests, α = 0.025) differences from two-sided tests against the

narrow condition: LME test (panel e) Wilcoxon signed rank (panels f, g) Wilcoxon ranked sum (panel h). Panel c was created in BioRender. Balla, E. https://BioRender.com/g05l789 (2025).

Figure 3. Gabor filter model links orientation tuning and surround suppression to broadband responses. (**a**) Schematic of a Gabor filter bank to model neural responses. Gabor filters of different orientations and spatial frequencies were used to jointly predict the measured responses to the presented broadband stimuli (see Fig. S3 and S4 for details). Model predictions were either based on the responses of a central Gabor alone ("tuning only" model; bottom left, yellow box) or by additionally accounting for the impact of surround suppression ("suppression" model; bottom right, red box) (**b**) Mean response amplitude towards narrow bandwidth stimuli, depending on the orientation tuning of V1 neurons (n = 11 sessions in 4 mice). Neurons in each session were binned based on their orientation tuning to a set of full-contrast sinewave gratings. Yellow circles and line show the best-fitted response of the tuning-only model. Red circles and line show the best fit of the suppression model. (**c**) Same as b) for broad orientation bandwidth stimuli. Both the tuning only and the suppression model were fit to narrow and broad orientation bandwidth stimuli at the same time. (**d**) Mean response modulation of orientation-tuned cells by expanding the orientation bandwidth (derived from responses in b and c). Yellow circles and line show the predicted response modulation from the tuning-only model. Red circles and line show predicted response modulation from the suppression model. The horizontal black dotted line at 0 indicates no bandwidth modulation. (**e**) Same as panel d) but for recruitment modulation of orientation-tuned cells by expanding the orientation bandwidth. The ORI recruitment modulation index was calculated as the difference between the numbers of responsive neurons to narrow and broad orientation bandwidth stimuli divided by their sum. Yellow and red circles indicate fits of the tuning only and surround suppression model, respectively. Box plots indicate the median (horizonal line), interquartile range (box bounds: 25th–75th percentiles), and whiskers (1.5× interquartile range). Stars in panels d and e mark significant differences against 0 based on an LME model (two-sided test). The significance threshold for each test was α = 0.01 after Bonferroni correction for five individual tests. Panel a was created in BioRender. Balla, E. https://BioRender.com/g05l789 (2025).

Figure 4. Broadband visual stimuli modulate neural responses by reducing surround suppression (**a**) Visual stimulation and imaging setup. (**b**) Example frames from each stimulus category. Stimuli had a central spatial frequency of 0.04 cpd and orientation of 0° and shown full-field or through a 15° circular aperture, centered on the receptive field of imaged neurons. Frame colors indicate the condition identity throughout the figure. (**c**) Raw coefficient correlations were computed as the central samples of the spatial auto-correlation of lowpass filtered stimuli. (**d**) Mean response amplitude difference versus baseline for each full-field stimulus condition. Shown are all neurons with a receptive field at the center stimulus and significant responses to any of the center stimulus conditions (378 out of 8210 neurons). The horizontal line shows the median for the narrow stimulus. (**e**) Same as panel d) but with responses to each center stimulus condition. (**f**) Surround modulation index for individual neurons, calculated as the difference between full-field responses in d) minus center stimulus response in e) divided by their sum. The horizontal line shows the median for the narrow stimulus condition. (**g**) Illustration of the linear mixed effects (LME) model with multiple regressors. Surround modulation, orientation tuning, and center responses were used to predict single-cell broadband modulation for each condition. The model also considers the mouse identity for each neuron (see Methods). (**h**) Explained variance of the full LME model for each stimulus condition and T statistics and *p* values for each regressor. Significant regressors are marked in red. (**i**) Polar plot to compare T statistics results for each stimulus condition. Each color-coded triangle shows the normalized T values for each regressor, indicating its respective contribution to the model prediction. Across all conditions, surround modulation was the most important predictor. Box plots indicate the median (horizonal line), interquartile range (box bounds: 25th–75th percentiles), and whiskers (1.5× interquartile range). Stars mark significant (Bonferroni correction for three tests, α = 0.0167) differences from two-sided tests against the narrow condition: Wilcoxon signed rank (panels d-f), LME test (panel i). For visualization only, outliers were excluded from distributions. Panels a and g were created in BioRender. Balla, E. https://BioRender.com/g05l789 (2025).

Figure 5. Broadband visual stimuli increase sensory responses in cortical and subcortical neurons (**a**) Overview of the widefield setup and example visual field sign map. Sign maps were used to confirm the anatomical alignment of recordings to Allen CCF (Wang, Q. et al. The Allen Mouse Brain Common Coordinate Framework: A 3D Reference Atlas. Cell 181, 936-953.e20 (2020)). Mice were head-fixed on a wheel and shown

the same protocol as in Fig. 4 on the right-side screen. (**b**) Widefield responses averaged over the 2s stimulus period. Mean responses to the narrow stimulus condition (top left) were subtracted from mean responses to broadband stimulus conditions. Shown are average response differences for SF stimulus condition (top right), ORI stimulus condition (bottom left), and mixed stimulus condition (bottom right). (**c**) Average response differences for the ORI stimulus condition across different visual cortical areas (n = 8 sessions from 4 mice). (**d**) Individual trial response amplitudes to each stimulus integrated over the 2s stimulus period (n = 408 trials from 4 mice). (**e**) Electrophysiological recordings. Left: Example brain slice from the V1 center, showing red fluorescence from the Neuropixels probe positioning. A scheme of the probe is placed next to the fluorescent trace to visualize the probe position during the recording (scale bar: 200 µm). Different depths are marked by dashed white lines. Right: LFP responses to each stimulus condition across different cortical depths. Colors show voltage changes after stimulus onset relative to baseline. Horizontal white lines show depth, as in the histology panel on the left. (**f**) The difference in LFP responses for each stimulus condition (SF, purple; ORI, dark blue; mixed, brown) compared to the LFP response to the narrow stimulus across depths. Error bars show mean and s.e.m. (n = 6 recordings from 3 mice). Box plots indicate the median (horizonal line), interquartile range (box bounds: 25th–75th percentiles), and whiskers (1.5× interquartile range). Stars in all panels mark significant differences from a two-sided LME model test against narrow. The significance threshold was α = 0.0167 after Bonferroni correction for performing three tests. For visualization only, outliers were excluded from distributions in panels c-d. Panel a was created in BioRender. Balla, E. https://BioRender.com/g05l789 (2025).

Figure 6. Expanding orientation bandwidth improves stimulus discriminability in V1 neurons

(**a**) Example field of view of an experiment with the central spatial frequency of 0.16 cpd and narrow or broad orientation bandwidth. Stimuli are shown at the bottom left of the plane, scale bar: 100 µm. (**b**) Number of responsive cells to broad orientation bandwidth (45°) with either 0.04 cpd or 0.16 cpd central spatial frequency, normalized to the respective number of cells responding to the narrow condition (5°). Data for 0.04 cpd are the same as in Fig. 1 and shown here for reference in gray. (**c**) Orientation modulation index, calculated as mean broad minus narrow orientation bandwidth responses, divided by their sum. Shown are all positively narrow and broad responding neurons for each central spatial frequency (n = 1333 responsive neurons for central SF = 0.04 cpd in gray, similar to data in Fig. S1c, n = 1345 responsive neurons for central SF = 0.16 cpd in blue. n = 4892 neurons in total across 18 sessions from 9 mice). (**d**) Discriminability between neural responses to stimuli with a central spatial frequency of either 0.04 cpd or 0.16 cpd. Shown is the discrimination index for narrow and broad orientation bandwidth in light and dark blue, respectively (n = 2096 neurons from 18 sessions). Shown are the results for all cells that responded to any of the presented stimuli. The horizontal black dotted line shows the median discriminability for the narrow-band. (**e**) Example field of view of an experiment with 90° central orientation and narrow or broad frequency bandwidth, scale bar: 100 µm. (**f-h**) Same as panels **(b-d)** but for narrow and broad frequency bandwidth and 0° and 90° central orientation. Box plots indicate the median (horizonal line), interquartile range (box bounds: 25th–75th percentiles), and whiskers (1.5× interquartile range). Stars in all panels mark significant (Bonferroni correction for two tests, α = 0.025) differences from a two-sided LME test against 1 (panels c, g) or the narrow bandwidth (panels b, d, f, h). For visualization only, outliers were excluded from distributions in panels b-d, f-h.

Figure 7. Expanding orientation bandwidth improves visual perception.

(**a**) Illustration of the visual discrimination task. The mouse initialized the trial by triggering the lick detection, followed by a 500-ms long ITI with a gray screen, followed by a visual cue (white cross) for 700 ms. Two stimuli were then shown next to each other, and the mouse had to touch one stimulus to report a choice. Mice then received a water reward at a central lick spout after touching the target stimulus. Triggering the lick detection (even if no reward was given) initiated the next trial. (**b**) Example stimuli for the spatial frequency discrimination task with different orientation bandwidths (left) and the orientation discrimination task with different spatial frequency bandwidths (right). (**c**) Spatial frequency discrimination performance for different orientation bandwidths. Spatial frequency discrimination performance was significantly higher for larger orientation bandwidth (n = 46 sessions from 6 mice). (**d**) Same as in panel c) but for the orientation discrimination performance with different spatial frequency bandwidth stimuli. (n = 25,17,19 sessions respectively.) (**e**) Psychometric curves for orientation discrimination performance at different target-distractor orientation differences. Colors show psychometric curves for different spatial frequency bandwidths. Expanding the spatial frequency bandwidth did not affect the maximal discrimination performance or discrimination thresholds. The horizontal dashed line shows the 72.7% discrimination threshold. Error bars are centered at the colored circles and show standard deviation (n = 30,18 and 24 sessions, respectively). (**f**) Discrimination thresholds for the three spatial frequency bandwidths showed no significant differences (n = 30, 18 and 24 sessions respectively). Box plots indicate the median (horizonal line),

interquartile range (box bounds: 25th–75th percentiles), and whiskers (1.5× interquartile range). Stars in panels c, d, and f show the significance of a two-sided Wilcoxon signed rank test against the narrow condition. The significance threshold was $\alpha = 0.025$ after Bonferroni correction for performing 2 tests. Panel a was created in BioRender. Balla, E. https://BioRender.com/g05l789 (2025).

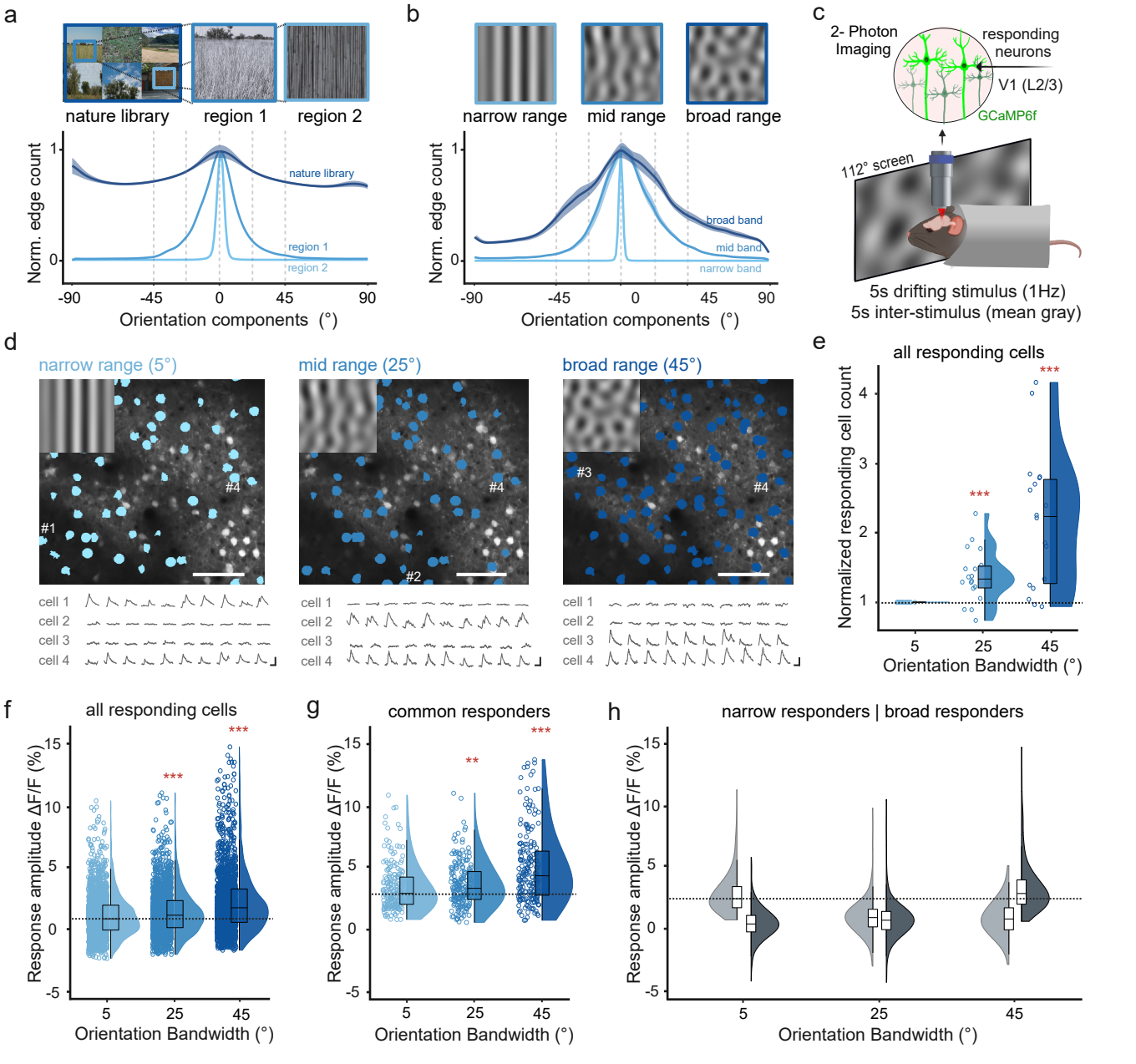
a
nature library
region 1
region 2
Norm. edge count
nature library
region 1
region 2
Orientation components (°)
b
narrow range
mid range
broad range
Norm. edge count
broad band
mid band
narrow band
Orientation components (°)
c
2- Photon Imaging
responding neurons
V1 (L2/3)
GCaMP6f
112° screen
5s drifting stimulus (1Hz)
5s inter-stimulus (mean gray)
d
narrow range (5°)
mid range (25°)
broad range (45°)
#1
#4
#2
#3
cell 1
cell 2
cell 3
cell 4
e
all responding cells
Normalized responding cell count
Orientation Bandwidth (°)
f
all responding cells
Response amplitude ΔF/F (%)
Orientation Bandwidth (°)
g
common responders
Response amplitude ΔF/F (%)
Orientation Bandwidth (°)
h
narrow responders | broad responders
Response amplitude ΔF/F (%)
Orientation Bandwidth (°)

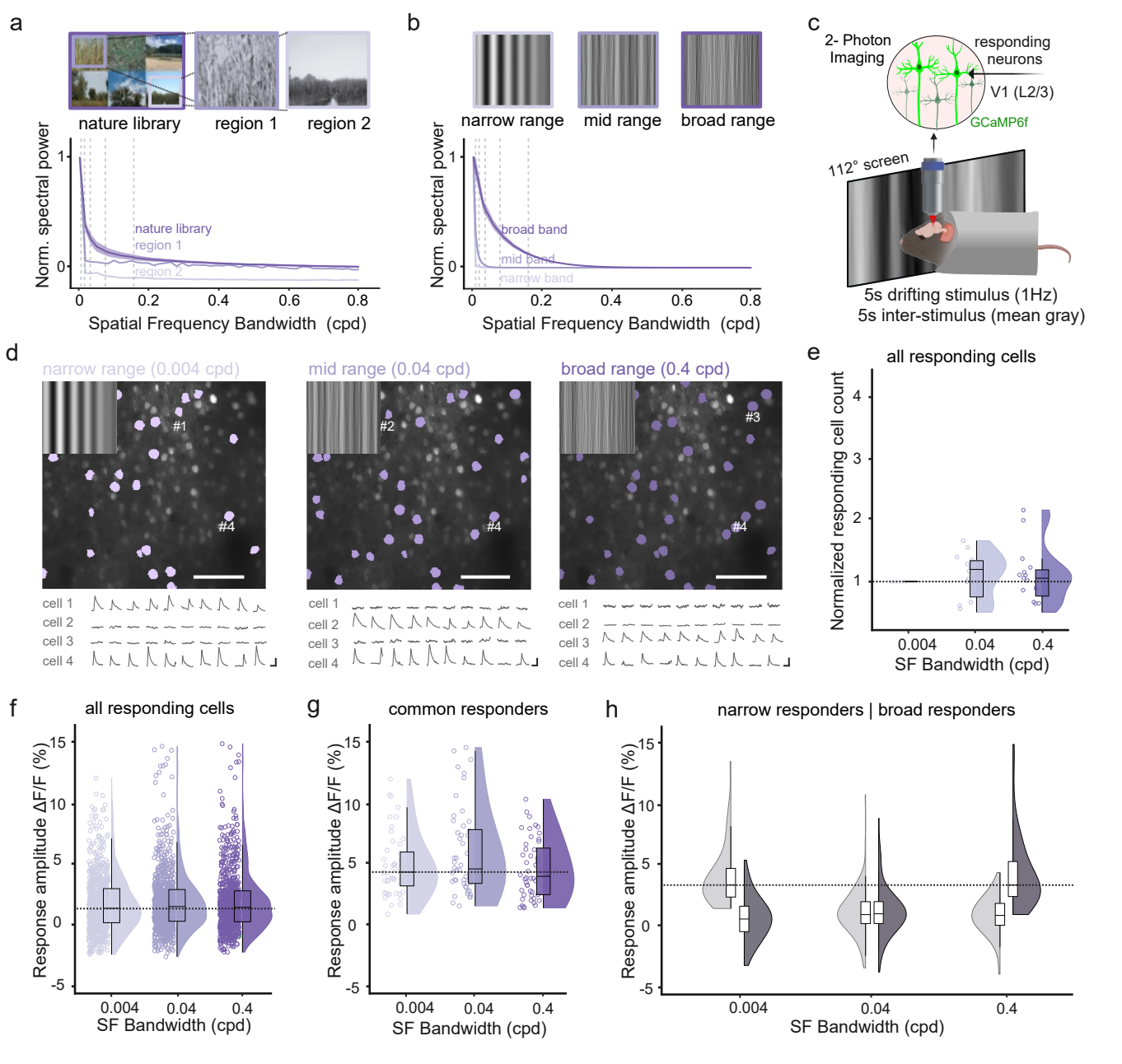
a
nature library
region 1
region 2
Norm. spectral power
nature library
region 1
region 2
Spatial Frequency Bandwidth (cpd)
b
narrow range
mid range
broad range
Norm. spectral power
broad band
mid band
narrow band
Spatial Frequency Bandwidth (cpd)
c
2- Photon Imaging
responding neurons
V1 (L2/3)
GCaMP6f
112° screen
5s drifting stimulus (1Hz)
5s inter-stimulus (mean gray)
d
narrow range (0.004 cpd)
mid range (0.04 cpd)
broad range (0.4 cpd)
#1
#2
#3
#4
cell 1
cell 2
cell 3
cell 4
e
all responding cells
Normalized responding cell count
SF Bandwidth (cpd)
f
all responding cells
Response amplitude ΔF/F (%)
SF Bandwidth (cpd)
g
common responders
Response amplitude ΔF/F (%)
SF Bandwidth (cpd)
h
narrow responders | broad responders
Response amplitude ΔF/F (%)
SF Bandwidth (cpd)

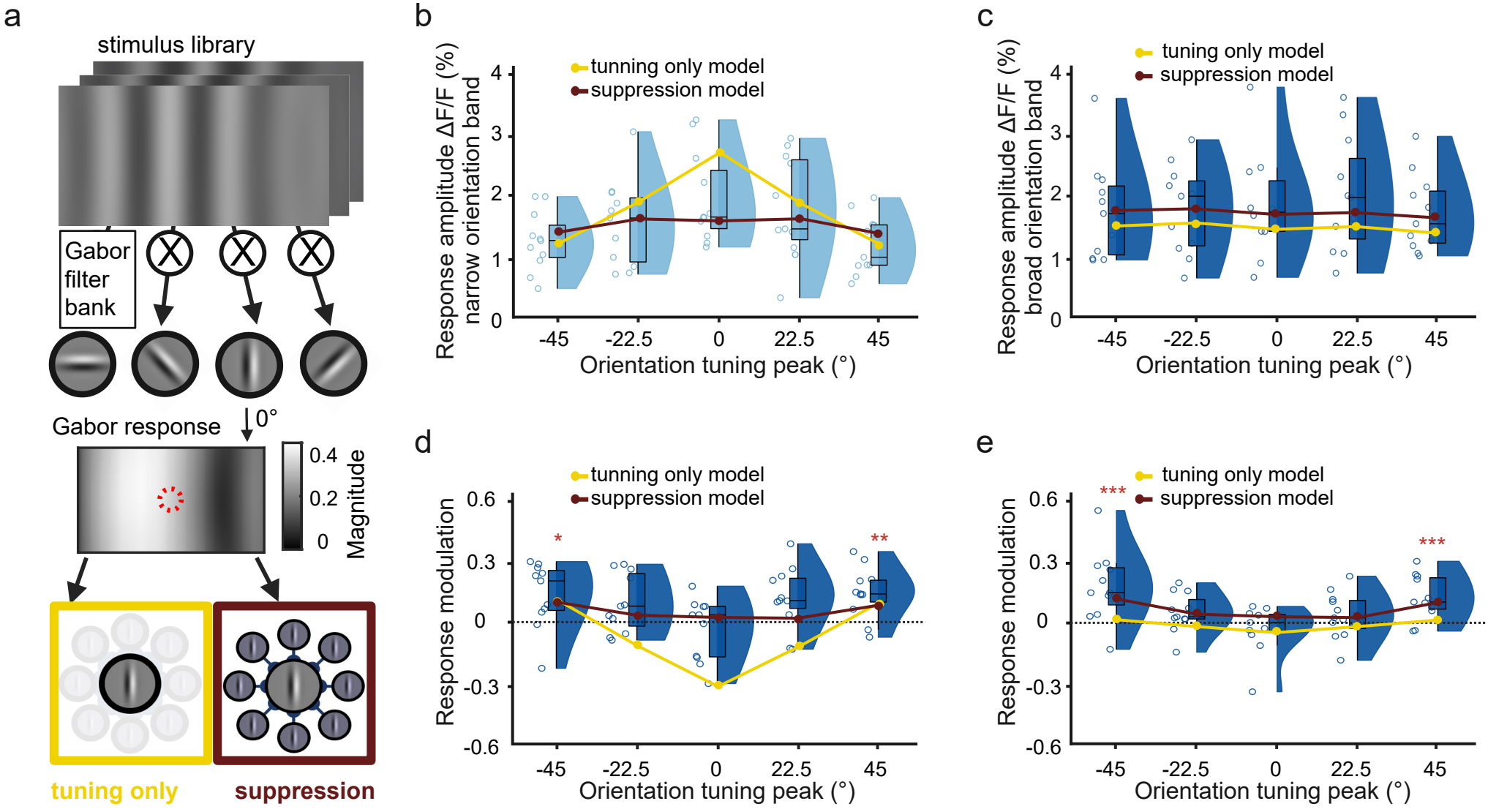
a
stimulus library
Gabor filter bank
Gabor response
0°
0.4
0.2
0
Magnitude
tuning only
suppression
b
tunning only model
suppression model
Response amplitude ΔF/F (%)
narrow orientation band
Orientation tuning peak (°)
c
tuning only model
suppression model
Response amplitude ΔF/F (%)
broad orientation band
Orientation tuning peak (°)
d
tunning only model
suppression model
Response modulation
Orientation tuning peak (°)
e
tuning only model
suppression model
Response modulation
Orientation tuning peak (°)

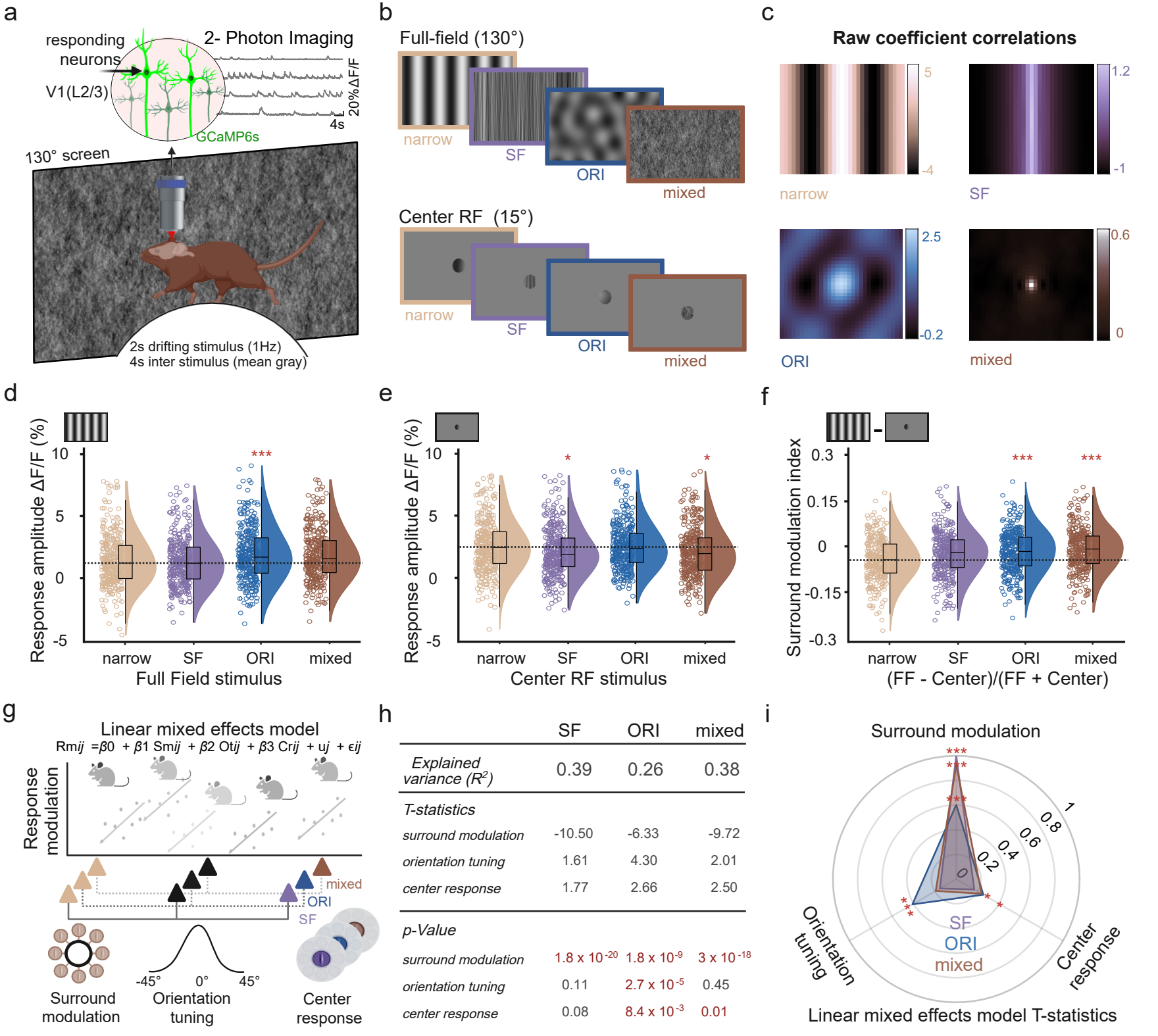

	SF	ORI	mixed
Explained variance (R^2)	0.39	0.26	0.38
T-statistics			
surround modulation	-10.50	-6.33	-9.72
orientation tuning	1.61	4.30	2.01
center response	1.77	2.66	2.50
p-Value			
surround modulation	1.8×10^{-20}	1.8×10^{-9}	3×10^{-18}
orientation tuning	0.11	2.7×10^{-5}	0.45
center response	0.08	8.4×10^{-3}	0.01

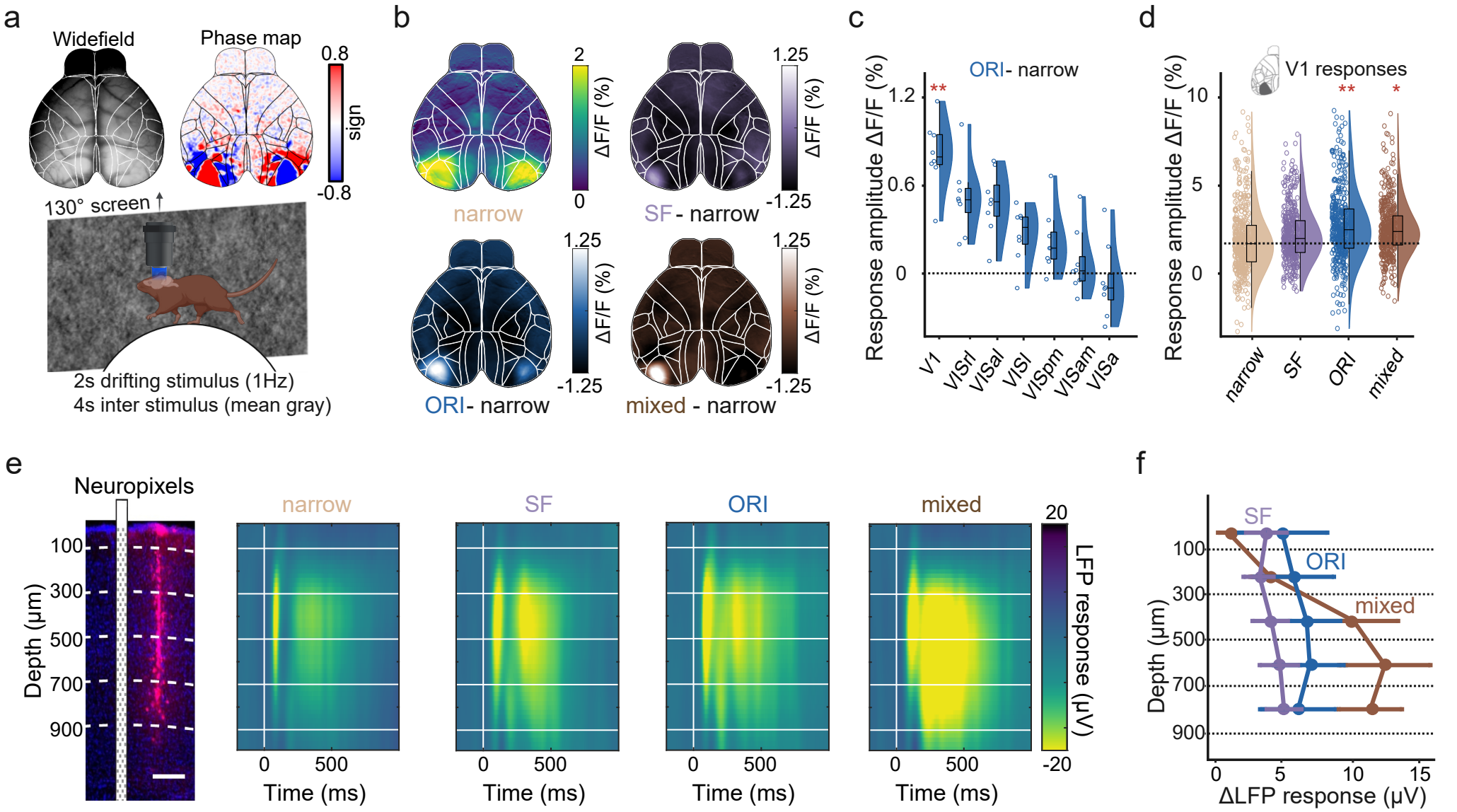
a
Widefield
Phase map
0.8
sign
-0.8
130° screen
2s drifting stimulus (1Hz)
4s inter stimulus (mean gray)
b
2
0
ΔF/F (%)
narrow
1.25
-1.25
SF - narrow
ORI- narrow
mixed - narrow
c
ORI- narrow
Response amplitude ΔF/F (%)
1.2
0.6
0
**
V1
VISrl
VISal
VISl
VISpm
VISam
VISa
d
V1 responses
10
5
**
*
narrow
SF
ORI
mixed
e
Neuropixels
Depth (μm)
100
300
500
700
900
narrow
SF
ORI
mixed
0
500
Time (ms)
20
-20
LFP response (μV)
f
SF
ORI
mixed
Depth (μm)
0
5
10
15
ΔLFP response (μV)

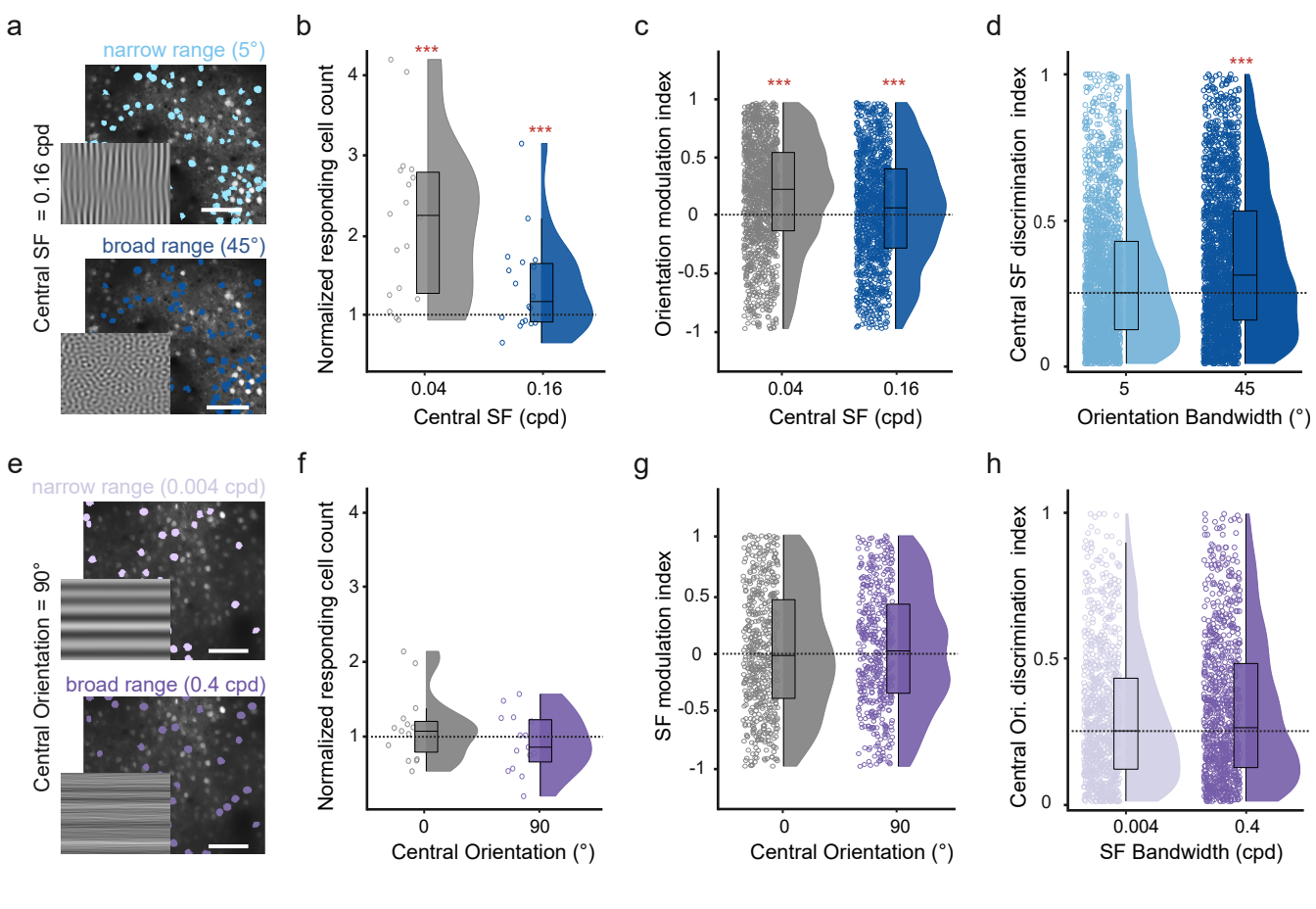
a
narrow range (5°)
broad range (45°)
Central SF = 0.16 cpd
b
Normalized responding cell count
***
***
0.04
0.16
Central SF (cpd)
c
Orientation modulation index
***
***
0.04
0.16
Central SF (cpd)
d
Central SF discrimination index
***
5
45
Orientation Bandwidth (°)
e
narrow range (0.004 cpd)
broad range (0.4 cpd)
Central Orientation = 90°
f
Normalized responding cell count
0
90
Central Orientation (°)
g
SF modulation index
0
90
Central Orientation (°)
h
Central Ori. discrimination index
0.004
0.4
SF Bandwidth (cpd)

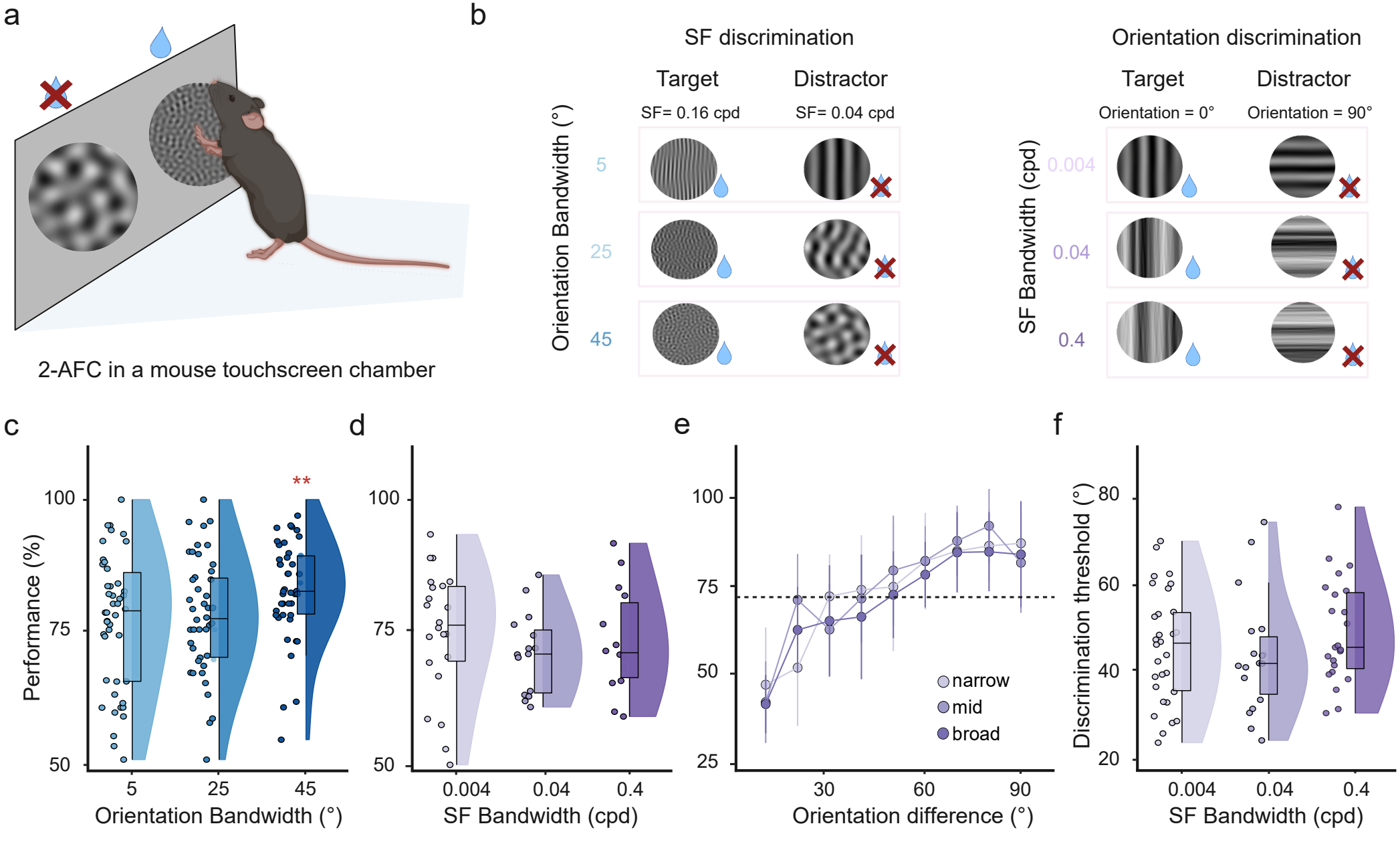
a
2-AFC in a mouse touchscreen chamber
b
SF discrimination
Target
Distractor
SF= 0.16 cpd
SF= 0.04 cpd
Orientation Bandwidth (°)
5
25
45
Orientation discrimination
Target
Distractor
Orientation = 0°
Orientation = 90°
SF Bandwidth (cpd)
0.004
0.04
0.4
c
Performance (%)
100
75
50
**
5
25
45
Orientation Bandwidth (°)
d
100
75
50
0.004
0.04
0.4
SF Bandwidth (cpd)
e
100
75
50
25
30
60
90
Orientation difference (°)
narrow
mid
broad
f
Discrimination threshold (°)
80
60
40
20
0.004
0.04
0.4
SF Bandwidth (cpd)